The GALAH Survey: using galactic archaeology to refine our knowledge of *TESS* target stars

Jake T. Clark [1][*] Mathieu Clerté,[1] Natalie R. Hinkel,[2] Cayman T. Unterborn,[3] Robert A. Wittenmyer,[1] Jonathan Horner,[1] Duncan J. Wright,[1] Brad Carter [1] Timothy D. Morton,[4] Lorenzo Spina [5] Martin Asplund,[6] Sven Buder [6,7] Joss Bland-Hawthorn [7,8] Andy Casey [5] Gayandhi De Silva,[5] Valentina D'Orazi,[9] Ly Duong,[6] Michael Hayden,[7,8] Ken Freeman,[6] Janez Kos,[7,10] Geraint Lewis [8] Jane Lin,[6] Karin Lind,[11] Sarah Martell [7,12] Sanjib Sharma,[8] Jeffrey Simpson [7,8] Dan Zucker,[13,14] Tomaz Zwitter [10] Christopher G. Tinney,[15,16] Yuan-Sen Ting (丁源森),[6,17,18,19] Thomas Nordlander [6,7] and Anish M. Amarsi [7,11]

[1] *Centre for Astrophysics, University of Southern Queensland, West Street, Toowoomba, QLD 4350, Australia*
[2] *Space Science and Engineering Division, Southwest Research Institute, San Antonio, TX 78238, USA*
[3] *School of Earth and Space Exploration, Arizona State University, Tempe, AZ 85287, USA*
[4] *Department of Physics and Astronomy, University of Southern California, Los Angeles, CA 90089, USA*
[5] *Monash Centre for Astrophysics, School of Physics and Astronomy, Monash University, VIC 3800, Australia*
[6] *Research School of Astronomy & Astrophysics, Australian National University, ACT 2611, Australia*
[7] *Center of Excellence for Astrophysics in Three Dimensions (ASTRO-3D), ACT 2611, Australia*
[8] *Sydney Institute for Astronomy, School of Physics, University of Sydney, NSW 2006, Australia*
[9] *INAF Osservatorio Astronomico di Padova, vicolo dell'Osservatorio 5, I-35122, Padova, Italy*
[10] *Faculty of Mathematics and Physics, University of Ljubljana, Jadranska 19, 1000 Ljubljana, Slovenia*
[11] *Max Planck Institute for Astronomy (MPIA), Koenigstuhl 17, D-69117 Heidelberg, Germany*
[12] *School of Physics, University of New South Wales – Sydney, Sydney 2052, Australia*
[13] *Department of Physics & Astronomy, Macquarie University, Sydney, NSW 2109, Australia*
[14] *Research Centre in Astronomy, Astrophysics & Astrophotonics, Macquarie University, Sydney, NSW 2109, Australia*
[15] *Exoplanetary Science at UNSW, University of New South Wales, Sydney, NSW 2052, Australia*
[16] *Australian Centre for Astrobiology,University of New South Wales, Sydney, NSW 2052, Australia*
[17] *Institute for Advanced Study, Princeton, NJ 08540, USA*
[18] *Department of Astrophysical Sciences, Princeton University, Princeton, NJ 08544, USA*
[19] *Observatories of the Carnegie Institution of Washington, 813 Santa Barbara Street, Pasadena, CA 91101, USA*

ABSTRACT

An unprecedented number of exoplanets are being discovered by the Transiting Exoplanet Survey Satellite (*TESS*). Determining the orbital parameters of these exoplanets, and especially their mass and radius, will depend heavily upon the measured physical characteristics of their host stars. We have cross-matched spectroscopic, photometric, and astrometric data from GALAH Data Release 2, the *TESS* Input Catalog and *Gaia* Data Release 2, to create a curated, self-consistent catalogue of physical and chemical properties for 47 285 stars. Using these data, we have derived isochrone masses and radii that are precise to within 5 per cent. We have revised the parameters of three confirmed, and twelve candidate, *TESS* planetary systems. These results cast doubt on whether CTOI-20125677 is indeed a planetary system, since the revised planetary radii are now comparable to stellar sizes. Our GALAH–*TESS* catalogue contains abundances for up to 23 elements. We have specifically analysed the molar ratios for C/O, Mg/Si, Fe/Si, and Fe/Mg, to assist in determining the composition and structure of planets with $R_p < 4R_{\oplus}$. From these ratios, 36 per cent fall within 2σ sigma of the Sun/Earth values, suggesting that these stars may host rocky exoplanets with geological compositions similar to planets found within our own Solar system.

Key words: methods: observational – catalogues – planets and satellites: interiors – stars: fundamental parameters – stars: abundances.

[*] E-mail: jake.clark@usq.edu.au

1 INTRODUCTION

Exoplanets (planets that exist beyond the Solar system) moved beyond science fiction and into the realm of hard science late in the 20th century (Latham et al. 1989; Lawton & Wright 1989; Wolszczan & Frail 1992; Mayor & Queloz 1995). From the first discoveries until the launch of the *Kepler* spacecraft, exoplanets were largely detected by radial velocity techniques, leading to a wealth of massive planet discoveries around largely Sun-like stars (e.g. Fischer et al. 2008; Vogt et al. 2010; Lovis et al. 2011; Wittenmyer et al. 2014; Endl et al. 2016).

Towards the end of the first decade of the 2000s, the transit technique became the numerically dominant method for making new exoplanet discoveries, and revealed an abundance of planets moving on very short period orbits (e.g. Noyes et al. 2008; Hellier et al. 2012; Muirhead et al. 2012; Rowe et al. 2014; Coughlin et al. 2016). The great advantage of transit observations over those using the radial velocity technique is that they permit surveys to target large numbers of stars simultaneously. The ultimate expression, to date, of the transit method as a tool for exoplanetary science came with the *Kepler* space telescope, launched in 2009 (Borucki et al. 2010).

At the time of writing, *Kepler* has been by far the most successful exoplanet detection program, discovering 65.5 per cent of currently known exoplanets.[1] These planetary discoveries have showcased the vast richness and diversity of exoplanets across our galaxy. The great diversity of exoplanets and exoplanetary systems is illustrated by the discovery of large numbers of multiplanet systems (e.g. Gillon et al. 2017; Shallue & Vanderburg 2018), planets in extremely eccentric orbits (e.g. Naef et al. 2001; Santerne et al. 2014; Wittenmyer et al. 2017), and planets that some have argued might resemble the Earth (e.g. Barclay et al. 2013; Torres et al. 2015).

The *Kepler* and K2 missions also revealed that planets larger than Earth, $>1R_\oplus$, yet smaller than Neptune, $<4R_\oplus$, are remarkably common – despite there being no such planets in the Solar system. Indeed, of those planets that we can readily detect, these 'super-Earths' and 'mini-Neptunes' seem to be by far the most common (Batalha et al. 2013). On 30 October 2018, the *Kepler* spacecraft depleted all of its on-board fuel, immediately retiring the mission and leaving behind a legacy that is unmatched in exoplanetary science. Fortunately, NASA's Transiting Exoplanet Survey Satellite (*TESS*) mission, launched in April 2018, has picked up where the K2 mission left off.

The *TESS* mission (Ricker et al. 2014) is a space-based photometric survey that will cover the entire sky, except for the region within ± 6 deg of the ecliptic plane. The mission is designed to find small planets ($R_p < 2.5R_\oplus$) around nearby, bright, main-sequence stars. As of 2020 August, there have been 66 confirmed planetary discoveries made as a result of *TESS'* ongoing survey (e.g. Huang et al. 2018; Nielsen et al. 2019b; Vanderspek et al. 2019; Addison et al. 2020; Gilbert et al. 2020; Jordán et al. 2020). In addition to the 66 confirmed *TESS* exoplanets, there are more than two thousand *TESS* Targets of Interest (TOI) and Community Targets of Interest (CTOI)[2] waiting for their exoplanetary status to be confirmed by ground-based teams (e.g Addison et al. 2019; Davis et al. 2019; Nielsen et al. 2019b; Wang et al. 2019a; Dalba et al. 2020; Eisner et al. 2020).

Once potential planets have been identified by *TESS*, the *TESS* Input Catalog (TIC) (Stassun et al. 2018; Stassun et al. 2019) and

Candidate Target List (CTL) are the key catalogues that enable follow-up teams to characterize – for both stars and planets – the members of *TESS* candidate systems. In particular, radial velocity data are needed to measure the planetary mass, and spectroscopic observations are needed to refine mass and radius of the host star. These measurements, in combination with the transit radius measurement from *TESS*, allow the bulk density of the planet in question, ρ_p,[3] to be determined, and thereby provide constraints on that planet's overall composition (Valencia, O'Connell & Sasselov 2006; Seager et al. 2007; Unterborn, Dismukes & Panero 2016).

Whilst the bulk density of a planet does provide clues to its potential bulk composition, it does not provide enough information for us to determine the geological structure of a potentially rocky planet, or to precisely determine its true composition. This is clearly illustrated by the work of Suissa, Chen & Kipping (2018), who demonstrate that a newly discovered 'Earth-like' planet (a planet observed to be both the same mass and the same size as the Earth; i.e. $1M_\oplus$, $1R_\oplus$) could have a wide variety of internal compositions. Distinguishing between the many possible compositions and structures of such a planet will be of great interest in the years to come, particularly in the context of the search for potentially habitable planets, and the selection of the most promising such planets for further study (e.g. Horner & Jones 2010).

Recent studies, however, have demonstrated that planetary scientists could potentially unlock the viscera of distant rocky worlds by combining our knowledge of the planets themselves with detailed information on the chemical abundances of their host stars (e.g. Bond, Lauretta & O'Brien 2010a; Bond, O'Brien & Lauretta 2010b; Dorn et al. 2015; Unterborn et al. 2016; Dorn et al. 2017a; Unterborn & Panero 2017; Hinkel & Unterborn 2018; Unterborn et al. 2018a; Dorn et al. 2019; Unterborn & Panero 2019). In particular, knowledge of the chemical abundances of refractory elements (such as Mg, Al, Si, Ca, and Fe) and volatile elements (such as C and O) can help us to determine the likely structure and composition of exoplanets smaller than $4R_\oplus$ (Dorn et al. 2019; Putirka & Rarick 2019).

The most crucial elements for such an analysis are C, O, Mg, Si, and Fe, as these elements will determine the core to mantle fraction (in particular Fe/Mg[4]) and the composition of a rocky exoplanet's mantle (e.g. Mg/Si and C/O, as per Bond et al. 2010b; Madhusudhan, Lee & Mousis 2012; Unterborn et al. 2014; Dorn et al. 2015; 2017a). Such models have recently proven vital in inferring the geological and chemical composition of the planets in the TRAPPIST-1 (Unterborn et al. 2018a), 55 Cnc (Dorn, Hinkel & Venturini 2017b), HD 219134 (Ligi et al. 2019), and other planetary systems.

As the catalogue of known exoplanets has grown, it has becoming increasingly obvious that our understanding of the planets we find is often limited by the precision with which we can characterize their host stars. In particular, measurements of the elemental abundances of exoplanet host stars are becoming increasingly important in developing our understanding of the fundamental synergies between stars and the planets they host. As a result, there is an increasing amount of research within exoplanetary science that aims to understand the relationship between a star's chemical abundances and the types of planets and planetary systems that they can form (e.g. Fischer &

---

[3] $\rho_p = M_p \left(\frac{4}{3} \pi R_p^3 \right)^{-1}$; where M_p and R_p are the planet's mass and radius, respectively.

[4] Stellar abundance ratios are calculated by $\left(\frac{X}{Y} \right)_\star = 10^{\left(\left[\frac{X}{H} \right]_\star + A(X)_\odot \right) - \left(\left[\frac{Y}{H} \right]_\star + A(Y)_\odot \right)}$.

---

[1] https://exoplanetarchive.ipac.caltech.edu/; accessed 2020 August 6 , counting discoveries from both *Kepler*'s primary mission, and the K2 survey.
[2] https://exofop.ipac.caltech.edu/tess/; accessed 2020 August 6.

Valenti 2005; Adibekyan et al. 2012; Buchhave et al. 2014; Buchhave & Latham 2015; Teske et al. 2019).

The relationship between planetary demographics and a star's measured photospheric iron abundance is a complex one. Over twenty years ago, studies showed that stars hosting hot-Jupiters (giant planets in very short period orbits) are typically iron-enriched compared to the Sun (Gonzalez 1997; Santos, Israelian & Mayor 2001; Fischer & Valenti 2005). This trend has, however, weakened in more recent studies (Osborn & Bayliss 2019; Teske et al. 2019). Similarly, the relationship between a star's iron abundance and the number of planets it hosts remains the subject of significant debate (e.g. Petigura et al. 2018; Adibekyan et al. 2017). Recent machine-learning work by Hinkel et al. (2019) has indicated that elemental abundances, including those of C, O, and Fe, can be used as a means to identify potential planet-hosting stars amongst the wider stellar population.

In addition to potentially helping us to understand the interior structure and composition of newly discovered exoplanets, recent work has also suggested that measurements of the elemental abundances of stellar photospheres and planetary atmospheres could also aid our investigation of the formation and migration history of the exoplanets we study. For example, Brewer, Fischer & Madhusudhan (2017) describe how measurements of an enhanced C/O ratio and [O/H] abundance in the atmospheres of ten hot Jupiters, compared to the equivalent abundances in their stellar hosts, serve as evidence that those planets must have formed beyond the water ice line, and that they must have then migrated inwards to reach their current location. In a similar fashion, studies of the composition and isotopic abundances of the planets and small bodies have long been used to attempt to disentangle their formation locations and migration histories (see e.g. Horner et al. 2020, and references therein). In summary, this recent work reveals that, if we are to fully characterize the exoplanets we discover, it is vital that we consider the elemental abundances of their host stars.

The Southern hemisphere's largest spectroscopic stellar abundance survey – the Galactic Archaeology with HERMES (GALAH) survey – is designed to investigate the stellar formation and chemical enrichment history of the Milky Way galaxy (De Silva et al. 2015; Martell et al. 2016; Buder et al. 2018). To do this, GALAH has collected high-resolution spectra for more than 600 000 stars, from which the abundances of up to 23 elements can be determined for each star. GALAH's latest public release, GALAH DR2 (Buder et al. 2018), contains the details of 342 682 stars for which both physical and chemical properties have been observed and derived.

In this work, we make use of the data in GALAH DR2 to calculate revised values for the mass and radius of 47 285 stars that have been cross-matched between GALAH DR2 and the TIC. We then calculate the C/O, Fe/Mg, and Mg/Si abundance ratios for those stars, providing a database of stellar abundances for potential planet hosting stars to facilitate future studies of the composition, structure, habitability, and migration history of exoplanets discovered by *TESS*.

In Section 2, we describe how GALAH DR2 is cross-matched with the *TESS* and *Gaia* catalogues (Section 2.1), before describing how we derive the characteristics for our stars through isochrone modelling (Section 2.2). We then go on to discuss the derivation of elemental abundances and abundance ratios for GALAH–*TESS* stars using GALAH DR2 (Section 2.3). The resulting physical and elemental parameters are then validated by comparison with other catalogs in Sections 3.1 and 3.2. In our discussion section, we examine our refined stellar and planetary parameters for

confirmed and candidate exoplanet host stars (Section 4.1) and the abundance ratio trends in our stellar sample (Section 4.2). Finally, we summarize our findings and draw our conclusions in Section 5.

2 METHODOLOGY AND DATA ANALYSIS

In this methodology section, we describe how we cross-matched the GALAH–*TESS* catalogue (Section 2.1), derived our physical stellar parameters including isochronic masses and radii from GALAH DR2 (Section 2.2), and calculated our [X/H] and X/Y abundance ratios using GALAH DR2 data (Section 2.3).

2.1 Cross-matching the CTL and GALAH catalogues

The *TESS* Input Catalog (TIC; Stassun et al. 2018; Stassun et al. 2019) presents the physical characteristics of stars that are likely to be observed during the primary *TESS* mission. Built before the launch of the spacecraft, the TIC uses photometric relationships to derive the physical properties of over 470 million point sources. Due to the large number of stars being observed by *TESS*, there is a selection process that gives a higher priority to stars that better suit the *TESS* mission goals, which are primarily to discover planets around bright, cool dwarfs (Ricker et al. 2014; Stassun et al. 2018). Stars within this subset of the TIC are a large component of the Candidate Target List (CTL), and are observed by *TESS* at a 2-min cadence, whilst the remaining targets are recorded at a 30-min cadence in the full-frame images (FFIs).

Several simulations of the exoplanetary outcomes of *TESS* have been produced, including Sullivan et al. (2015) and Barclay, Pepper & Quintana (2018). Sullivan et al. (2015) predicted that *TESS* will discover 20 000 planets over the next 2 yr (1700 from CTLs and the rest from full-frame images). A more conservative yield prediction by Barclay et al. (2018) estimates that 1250 exoplanets will be discovered orbiting CTL stars, with an additional 3100 being found orbiting stars within the full-frame images. Both sets of simulations suggest that a large number of planets will discovered by *TESS*, from both the CTL and full TIC samples.

The most recent data release from GALAH (DR2; Buder et al. 2018) contains data derived from high resolution spectra for a total of 342 682 southern stars. Stars in the GALAH DR2 were first cross-matched with *Gaia*'s second data release (DR2; Gaia Collaboration et al. 2018), using the TOPCAT (Taylor 2005) tool to match GALAH and *Gaia* sources with a position tolerance of ±1 arcsec, providing *Gaia*-band magnitudes and parallaxes for our isochronic models. The returned stars were then cross-matched against release 8.0 of the TIC[5] using 2MASS (Skrutskie et al. 2006) identifiers from the GALAH catalogue, accessed through the Mikulski Archive for Space Telescopes `astroquery`'s API (Ginsburg et al. 2019).

For our catalogue, we selected GALAH DR2 stars with a high signal-to-noise ratio (S/N) across all four of HERMES's CCDs, only accepting stars that had a S/N ratio value of 50 or higher in each wavelength band. We also omit stars with a `flag_cannon` greater than zero, which indicates some problem in the data analysis, from our data set. The flagging scheme utilized in GALAH DR2 is described in greater detail in Buder et al. (2018).

For completeness, we compared the *Gaia* G-band magnitude from the TOPCAT cross-match to the same value found in the CTL catalogue. These values should be identical to one another, and hence

---

[5] https://filtergraph.com/tess_ctl; accessed 2020 August 6.
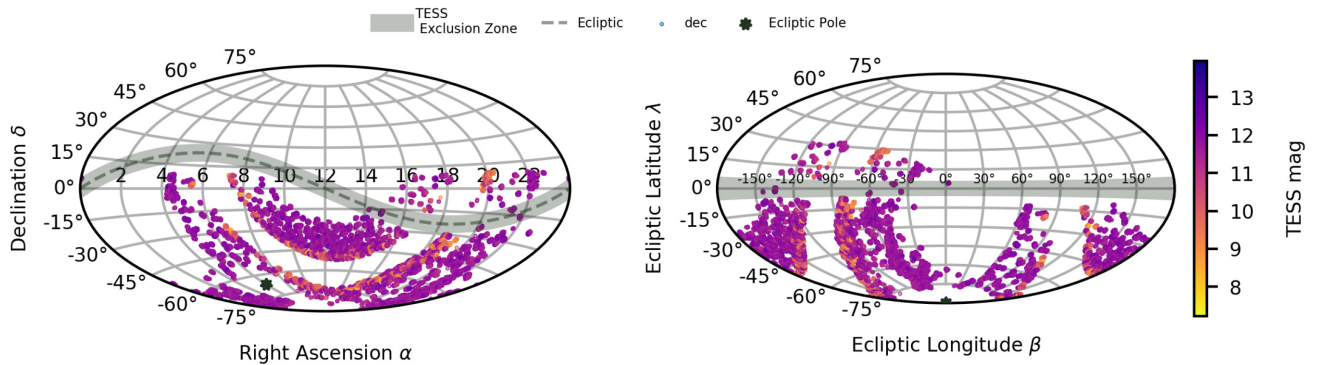
Figure 1. Aitoff projection of GALAH–*TESS* stars in both equatorial (right ascension and declination) and ecliptic (latitude and longitude) co-ordinates. The ecliptic plane, southern ecliptic pole, and *TESS* exclusion zone are shown in each (except for the ecliptic from the ecliptic co-ordinate plot as it corresponds to $\lambda = 0°$). Stars that are observed with HERMES within *TESS*'s Continuous Viewing Zone are a part of the TESS-HERMES survey, and thus not observed with GALAH. Stars within the *TESS* exclusion zone have been left within the GALAH–*TESS* catalogue, as these stars may be observed in the future with *TESS*.

serve as confirmation that we have the correct stars cross-matched within our catalogue. We considered a match to be confirmed if the difference in a star's celestial coordinates was less than 0.0001 deg and the difference in 2MASS J–H colour magnitudes (J–H) was also below 0.0001 mag for the exoplanet hosts.

We also wanted to include in our GALAH–*TESS* sample any stars that may have slightly lower S/N spectra in GALAH, but which are known to host either a confirmed exoplanet, a *TESS* TOI, or a CTOI. We accessed the *TESS* Follow-up Observing Program and NASA's EXOFOP-TESS data bases, and cross-matched them with GALAH DR2 and *Gaia* DR2. Our cross-match approach was simpler for these targets, as we merely needed to match them by their TIC IDs. There was only one star cross-matched within the CTOI list that had its S/N less than 50, this being UCAC4 306-282520. This star's green and blue channels have S/N values of 32 and 42, respectively.

Taking all of the above into consideration, our newly formed GALAH–*TESS* catalogue boasts 47 285 stars across the southern night sky, as shown in Fig. 1. Of these 47 285 stars, 2260 are prioritized sufficiently highly by the *TESS* mission that they are included in the TIC's CTL catalogue, being observed with a higher cadence relative to other stars in the general TIC. Fig. 2 shows the distributions of our GALAH–*TESS* stars as a function of their *TESS* and *V*-band magnitudes. The median *TESS* magnitudes for our CTL and TIC stars are 11.4 and 12.5, respectively, whilst the median V-band magnitudes for our CTL and TIC stars are 10.7 and 11.9, respectively. The slightly lower median values for stars on the CTL compared to those for the general TIC reflect *TESS*'s primary mission objectives, prioritizing brighter stars.

Due to flexible constraints by which we cross-matched the catalogues, there are GALAH–*TESS* stars that are located within the ecliptic, with a *TESS* priority of zero, that will not be observed within the initial 2 yr *TESS* primary mission. We have left those stars in our GALAH–*TESS* catalogue, as they might be explored during the *TESS* extended mission, following the conclusion of the primary survey. There is a large, deliberate absence of stars surrounding the *TESS* Continuous Viewing Zone, with no star within our catalogue being found at ecliptic latitudes south of $-78°$, in order to avoid any crossover of stars being observed and analysed by the TESS-HERMES Survey (Sharma et al. 2018). There are also no stars in our catalogue which overlap fields observed as part of the K2 survey, in order to avoid any potential crossover with the K2-HERMES survey (Wittenmyer et al. 2018; Sharma et al. 2019).

2.2 Deriving stellar radii and masses from GALAH stellar parameters

Details on the observation strategy and data pipeline for GALAH DR2 can be found in Kos et al. (2017), Martell et al. (2016), and Buder et al. (2018). Briefly, all GALAH DR2 observations are acquired with the 3.9 m Anglo-Australian Telescope situated at the Siding Spring Observatory, Australia. The two degree-field prime focus top-end (2dF; Lewis et al. 2002) with 392 science fibres is used to feed the High Efficiency and Resolution Multi Element Spectrograph (HERMES; Sheinis et al. 2015), delivering high resolution ($R \approx 28\,000$) spectra in four wavelength arms covering 471.3–490.3, 564.8–587.3, 647.8–673.7, and 758.5–788.7 nm.

The spectra for each star are corrected for systematic and atmospheric effects and then continuum normalized. Detailed physical parameters, including effective temperature ($T_{\rm eff}$), surface gravity ($\log g$), global metallicity ([M/H]), and individual abundances ([X/Fe]), have been determined for 10 605 selected stars using 1D stellar atmospheric models via the Spectroscopy Made Easy (Valenti & Piskunov 1996) package. Both the spectroscopic information and stellar parameters for these 10 605 stars then form a training set for the machine-learning algorithm *The Cannon* (Ness et al. 2015), which is used to train a data-driven spectrum model algorithm on the entire GALAH DR2 survey. Flags are produced by *The Cannon*'s processing for the 'quality' of the derived physical parameters in each star. For our analysis, we only include stars in the GALAH–*TESS* catalogue if they have a '0' flag_cannon in the GALAH DR2 release.

To derive the mass, radius, and ages of our GALAH–*TESS* stars, we used the PYTHON package isochrones (Morton 2015). The isochrones code uses MESA Isochrones & Stellar Tracks (MIST; Choi et al. 2016) stellar evolution grids to infer the physical characteristics of stars. For this analysis, we used as input observables: the star's effective temperature ($T_{\rm eff}$), surface gravity ($\log g$), 2MASS (J, H, K_s), and *Gaia* (G, $G_{\rm RP}$, $G_{\rm BP}$) photometric magnitudes, along with parallax values obtained by *Gaia* DR2 (Gaia Collaboration et al. 2018) where available.

Isochrone models rely on knowledge of a star's global metallicity, [M/H]. The assumption that the iron abundance [Fe/H] can be a proxy (or even equal) to [M/H] breaks down for metal-poor stars (e.g. Fuhrmann 1998; Reddy, Lambert & Allende Prieto 2006; Adibekyan et al. 2012, 2013a; Recio-Blanco et al. 2014). The radiative opacity of metal poor stars can be heavily affected by Mg, Si, Ca, and Ti
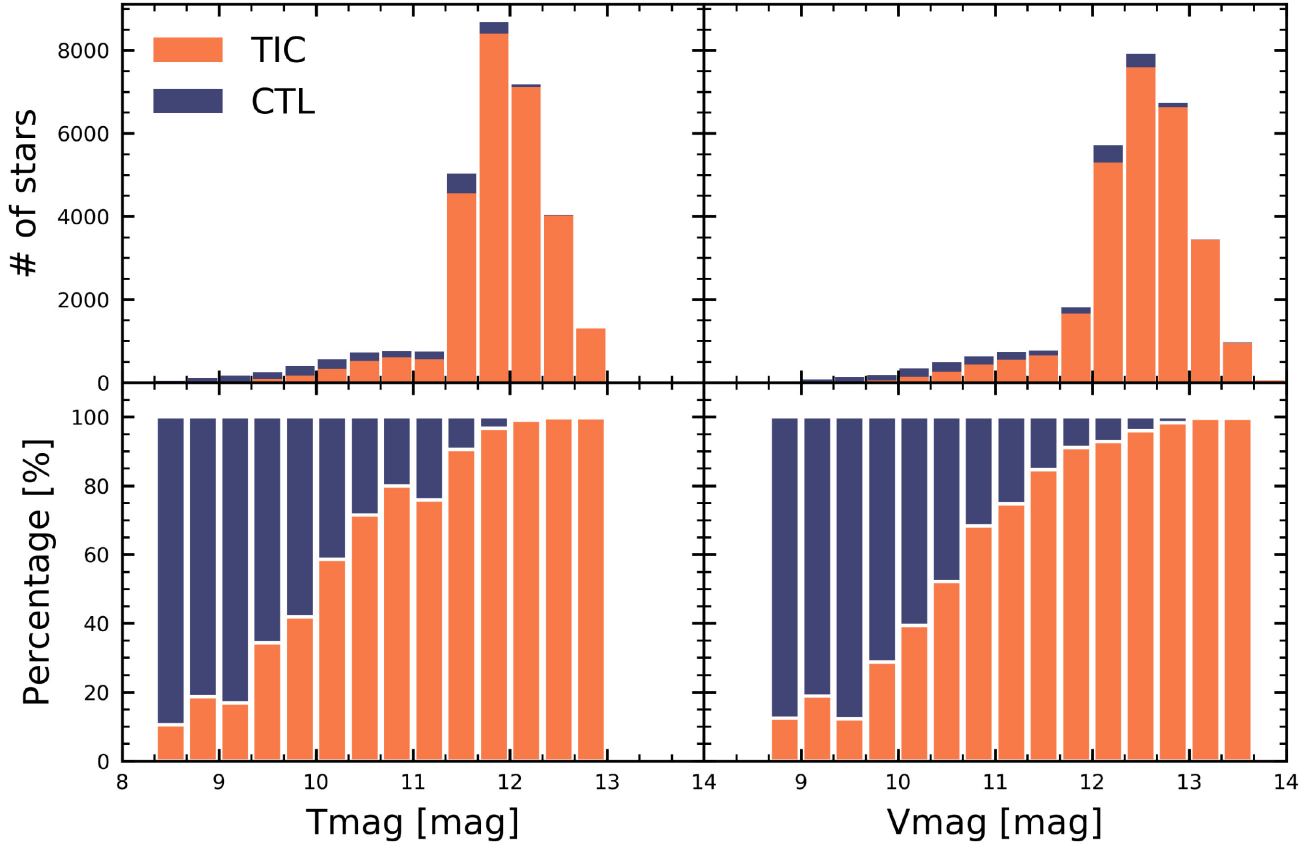
Figure 2. Of the 47 285 stars that are included in both the GALAH DR2 catalogue and the *TESS* input catalogue (TIC), 2260 are members of the Candidate Target List (CTL; shown here in purple), and are scheduled to be observed with a higher cadence relative to stars within the general TIC (orange). Left: Of the 2260 CTL stars, 650 stars are brighter than a *TESS* magnitude (T_{mag}) of 10, 1527 lie between T_{mag} 10 and 12, and 83 with a T_{mag} between 12–14. The median *TESS* magnitudes for our CTL and TIC stars are 11.4 and 12.5, respectively. The top plot shows the number of TIC and CTL members in each bin whilst the bottom plot shows the percentage of stars in each magnitude bin that belong to the TIC and CTL, respectively. Right: Of the 2260 CTL stars, 299 stars are brighter than a *V* magnitude of 10, 1099 lie between *V* magnitudes of 10–12, and 862 have a *V* magnitude between 12 and 14. The median *V* magnitudes for our CTL and TIC stars are 10.7 and 11.9, respectively. The slightly lower median values for CTL values compared to the TIC reflect *TESS*'s primary mission objectives, prioritizing brighter stars. The significant increase in the number of stars between *V*mag 12.0–13.7 and T_{mag} 11.3–13.0 reflects GALAH's observing strategy.

(i.e. by α-elements). Including these α-elements in our calculations of global metallicity better predicts the physical parameters derived with `isochrones`. GALAH DR2 calculates an [α/Fe] value for each star using equation (1):

$$[\alpha/\text{Fe}] = \frac{\sum \frac{[\text{X/Fe}]}{(\text{e\_[X/Fe]})^2}}{\sum (\text{e\_[X/Fe]})^{-2}}, \tag{1}$$

where X = Mg, Si, Ca, and Ti and e_[X/Fe] is the abundance's associated uncertainty. [α/Fe] will be calculated even if one or more of these elements are missing. From our iron abundance, [Fe/H], and [α/Fe], we can then calculate [M/H] using Salaris, Chieffi & Straniero (1993):

$$[\text{M/H}] = [\text{Fe/H}] + \log_{10} \left(0.638 f_\alpha + 0.362 \right), \tag{2}$$

where f_α is the α-element enhancement factor given by $f_\alpha = 10^{\left[\frac{\alpha}{Fe}\right]}$. Our calculated [M/H] value is then used in the isochrone modelling of each star.

When using `isochrones`, if a star failed to converge, it was omitted from our catalogue. Of our original 47 993 stars, 708 stars failed to converge, leaving the 47 285 stars that comprise the GALAH–*TESS* catalogue. When the model reached convergence,

the median output values of the stellar mass, radius, density, age, and equivalent evolution phase, as well as their corresponding 1σ uncertainties are calculated from the posterior distributions. We calculate stellar luminosity through the Stefan–Boltzmann relationship, and use those luminosities to derive the five habitable zone distances for each star, as formulated by Kopparapu et al. (2013). GALAH DR2 rotational, radial, and microturbulence velocities have been included in the GALAH–*TESS* catalogue to assist ground-based radial velocity teams to better prioritize follow-up targets.

2.3 Deriving stellar abundances and ratios for GALAH–*TESS* stars

In addition to providing the physical parameters for over 47 000 stars, our catalogue also contains the chemical parameters that could prove vital in determining the composition of rocky planets potentially hosted by these stars. Stellar elemental abundances for 23 elements, as well as quality flags, are derived from *The Cannon*, with the details of the derivation of these abundances their associated systematics discussed in detail in Buder et al. (2018). To ensure that we deliver to the community a usable catalogue, we have removed values with [X/Fe] flags not equal to zero.
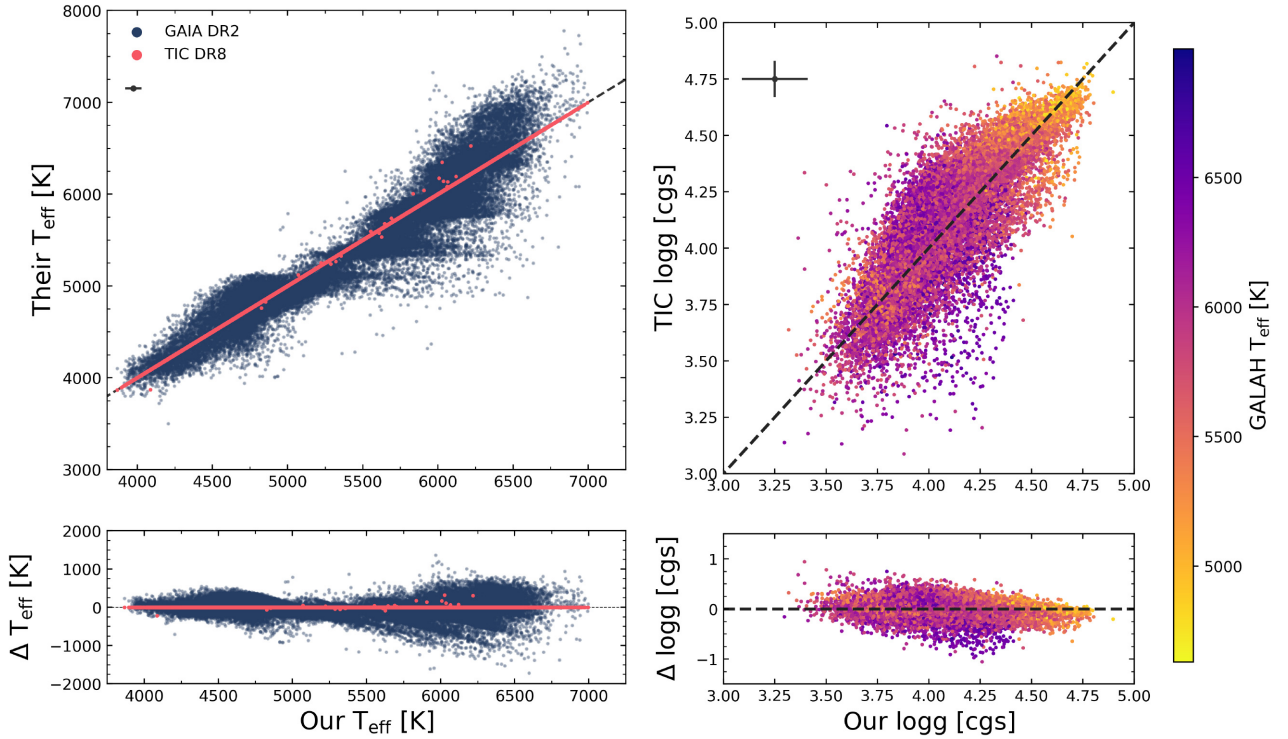
Figure 3. Left: Comparing the GALAH derived effective temperatures, with those published by *Gaia* DR2 (blue) and TIC DR8 (pink) for our GALAH-*TESS* sample of 47.974 stars. The GALAH DR2 effective temperatures have been included within the TIC, indicated by scatter points lining up on top of the equality line (black dashed line). With our cross-matching methodology, *Gaia* DR2's data set does not contain T_{eff} errors, and hence not visible within the plot. Right: Comparing the GALAH and TIC derived surface gravities with each star colour coded by its effective temperature. Only ∼60 per cent of CTL stars within our GALAH–*TESS* sample have measured surface gravity measurements. Error bars for both figures have been suppressed due to clarity; however, a median error bar is shown in the figures' top-left corner.

Whilst GALAH DR2 has its own internal Solar normalization, we have converted our elemental abundances from a GALAH normalized scale to Lodders, Palme & Gail (2009), and moved the abundances from being normalized by iron to hydrogen [X/H], since such values are more widely used within the current exoplanetary community. The derived Mg/Si, Fe/Mg, and C/O ratios were all calculated using our [X/H] stellar abundances and Lodders et al. (2009) Solar normalizations, where available.

3 RESULTS

Our results section is split into two separate parts, which detail the in-depth results of both the physical (Section 3.1) and chemical (Section 3.2) characteristics of stars within our GALAH–*TESS* catalogue, and provide comparisons of those results to other surveys and catalogues.

3.1 Atmospheric and physical characteristics of GALAH–*TESS* stars

The current TIC incorporates data from large, ground-based spectral surveys including LAMOST (Cui et al. 2012), RAVE (Steinmetz et al. 2006), TESS-HERMES (Sharma et al. 2018), and GALAH. For the vast majority of stars in our sample, the TIC has incorporated GALAH DR2 effective temperatures, which can be see as a line of equality in Fig. 3. Our GALAH–*TESS* temperatures, which have a median error of 54 K, seem to be in reasonable agreement with *Gaia*'s, with a larger scatter for hotter stars than for cooler stars.

There tends to be a slightly better agreement with *Gaia*'s T_{eff} for stars slightly cooler than the Sun (4750 ≤ GALAH–*TESS* T_{eff} ≤ 5500) with an rms of 146 K and median bias of 50 K, compared to the hotter stars (T_{eff} > 5500), and cooler stars (T_{eff} < 4750), with rms values of 168 and 253 K and median bias values of 34 and 25 K, respectively. The high scatter in results for the hotter stars is to be expected, with (Buder et al. 2018) noting an underestimate of GALAH T_{eff} values for hotter *Gaia* benchmark stars, which might be due to GALAH's input training set preferentially favouring cooler temperatures. There are horizontal structures between 5250 and 5750 K for *Gaia* T_{eff} values compared to those obtained using GALAH data. Similar structures were found by Hardegree-Ullman et al. (2020) when comparing *Gaia* T_{eff} values with spectral values obtained with LAMOST. These structures suggest that the *Gaia* temperature calculations in this range tend to certain preferred temperatures, which may be the result of *Gaia*'s input training set.

Because the TIC prioritizes stars being observed with a 2-min cadence (the CTL), surface gravities are only presented within the TIC for stars with a log g > 3. In addition, the TIC does not include derived log g values from other surveys, opting instead for a homogeneous data set to ensure internal consistency with their mass and radius values. In our cross-matched sample, we include both dwarfs and giants, since giant stars are also known to be planet hosts (Johnson et al. 2011; Jones et al. 2016; Huber et al. 2019; Wittenmyer et al. 2020). As a result, Fig. 3 only shows the comparison for GALAH–*TESS* stars that have both measured log g values in both catalogues. For our sample of main-sequence stars that have TIC log g values, the agreement between their log g values
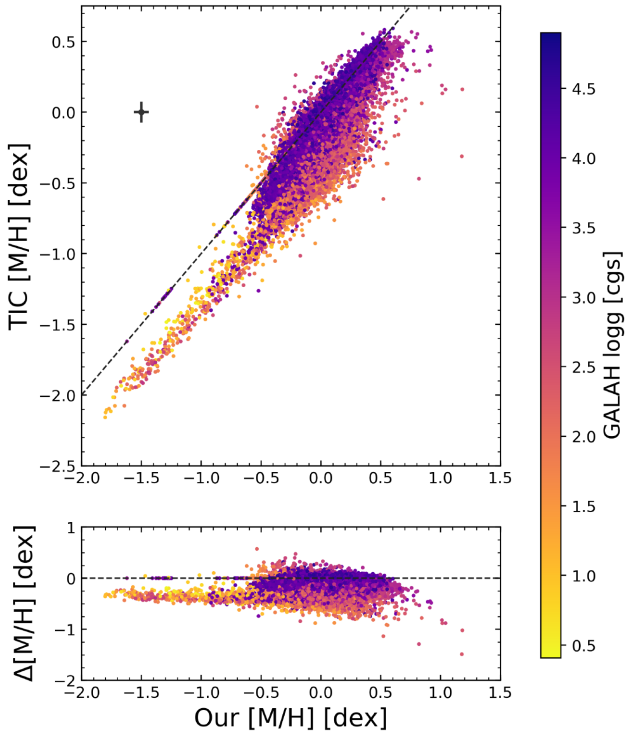
Figure 4. Comparing GALAH's global metallicity [M/H] to that of the TIC, with the colour of each star colour denoting its surface gravity, as derived by GALAH. The median error bar is given by the grey point to the figure's top-left corner, with an equality line given by the dark grey dashed line. The TIC directly uses GALAH DR2's [Fe/H] as [M/H], which this equality holds for thin-disc and alpha-poor stars. However, for thick-disc and alpha-rich stars, this equality does not hold true. From this figure, the median difference between [M/H] and [Fe/H] for alpha-rich stars is ∼0.3 dex. Since isochronic evolutionary tracks depend on [M/H], this assumption of [M/H] = [Fe/H] would have given less accurate mass, radius, and age results for our alpha-rich stars. For a small portion of our stars, there was no [α/Fe] abundance, and hence, we use [Fe/H] as [M/H] in our isochrone models for these specific stars.

and ours appears reasonable, with an rms and median bias of 0.14 and −0.03 dex, respectively, compared to the median GALAH log *g* error of 0.16 dex. In comparison, the TIC's median error bar is only 0.08 dex.

The TIC's global metallicity values, [M/H], have mostly been acquired from the large, ground-based surveys such as LAMOST, RAVE, etc. (Cui et al. 2012; Steinmetz et al. 2006). For those stars for which the TIC used GALAH DR2 parameters, they directly incorporated GALAH's [Fe/H] as the TIC's [M/H]. This equality does hold for metal-rich stars. However, there is a large discrepancy between [M/H] and [Fe/H] for thick-disc and metal-poor stars that are enriched in α-elements. These α-elements affect the radiative opacity of iron-poor stellar surfaces, with the overall metallicity and iron abundance equality breaking down within this regime. If the overall metallicity does not take into account the α-abundance, [α/Fe], for iron-poor stars, this could drastically alter the star's derived isochrone track. This in turn would alter the final stellar parameters that are produced with this model.

If we wish to better characterize stars observed with *TESS*, we therefore need to take [α/Fe] into consideration, as we did in Section 2.2. Fig. 4 shows the comparison between the overall metallicities taken from the TIC, and those calculated using GALAH data. There are 317 stars that do not have a [α/Fe] measurement, and

for those stars, we simply equated their iron abundance to the overall stellar metallicity. The rms and bias between the TIC and GALAH's overall metallicity is 0.18 and 0.08 dex, respectively. As we expected, however, the rms between the two data sets is significantly lower for alpha-poor stars ([α/Fe] < 0.1), with an rms and bias values being 0.08 and 0.05 dex, respectively. There is a much larger difference in [M/H] for iron-poor/alpha-rich stars, which is to be expected, with an rms and bias of 0.32 and 0.27 dex, respectively. For comparison, the median error in the derived [M/H] values is 0.07 dex.

GALAH's T_{eff}, log *g* and [M/H] values together with the astrometric and photometric observables are fed into the ISOCHRONES code, producing the radius and mass values which are depicted in Fig. 5. Our radii show good overall agreement with both *Gaia* DR2 and TIC. However, at large radii (giant stars), our calculated radii tend to be smaller than those taken from the TIC and *Gaia*. The median relative error for our stellar radii is 2.7 per cent, with the relative RMS between our results and those of *Gaia* DR2 and TIC found to be 10 per cent and 14 per cent, respectively. Our median stellar radius value is 1.89 R_⊙, which is comparable to the median values of the *Gaia* and TIC data of 1.84 R_⊙ and 1.92 R_⊙, respectively.

The general agreement between our results and the radii derived by *Gaia* and the TIC is not unexpected, since our ISOCHRONES models rely on *Gaia* DR2's photometric magnitudes and parallax values. The TIC's methodology is similar in that it also relies on data from *Gaia* to derive its stellar radii values. These stellar radii values will prove fundamental in calculating planetary radii for exoplanet host stars discovered by *TESS* within our sample.

Ground-based follow-up teams mostly rely upon the radial velocity method to confirm TOIs (e.g Addison et al. 2019; Davis et al. 2019; Nielsen et al. 2019b; Wang et al. 2019a; Dalba et al. 2020; Eisner et al. 2020). From this methodology, it is possible to infer the planetary mass through the radial–velocity semi-amplitude. However, the planetary mass is inferred based on our knowledge of the mass of the host star. It is therefore important to not only determine and refine the stellar radii of GALAH–*TESS* stars, but to also refine their masses. Over 40 per cent of our sample do not have TIC stellar mass values, as they are giant stars and prioritised less than their dwarf counterparts by *TESS*.

Included within Fig. 5 is the comparison between our derived isochronic masses and those contained within the TIC. In our total sample, the median stellar mass is 1.21 M_⊙, compared to a slightly smaller mass of 1.11 M_⊙ for the subset of stars with mass measurements in the TIC. This is to be expected, since the TIC only includes mass measurements for dwarf stars. Our masses are slightly larger than those within the TIC, with a median increase of 11 per cent between our mass measurements and those in the TIC. This increase is slightly larger than our median relative error in stellar mass, being roughly 4 per cent. However, our median uncertainty is significantly smaller than that found within the TIC, with their median relative uncertainty being 13 per cent.

A Hertzsprung–Russell diagram of our results is shown in Fig. 6, based on GALAH DR2 T_{eff}, log *g*, and ISOCHRONES-derived stellar luminosity. This sanity check confirms that none of our GALAH-*TESS* stars fall in unphysical regions of the H–R diagram parameter space. Using the definitions used in Sharma et al. (2018), hot dwarfs dominate the GALAH–*TESS* catalogue, accounting for 62 per cent of the stars (with 38 per cent being giant stars). A very small fraction of our sample are cool dwarfs, with only 52 such stars. This number of cool dwarf stars is consistent with GALAH being a magnitude-limited survey and the *TESS* goals of detecting exoplanets primarily around bright, nearby stars.
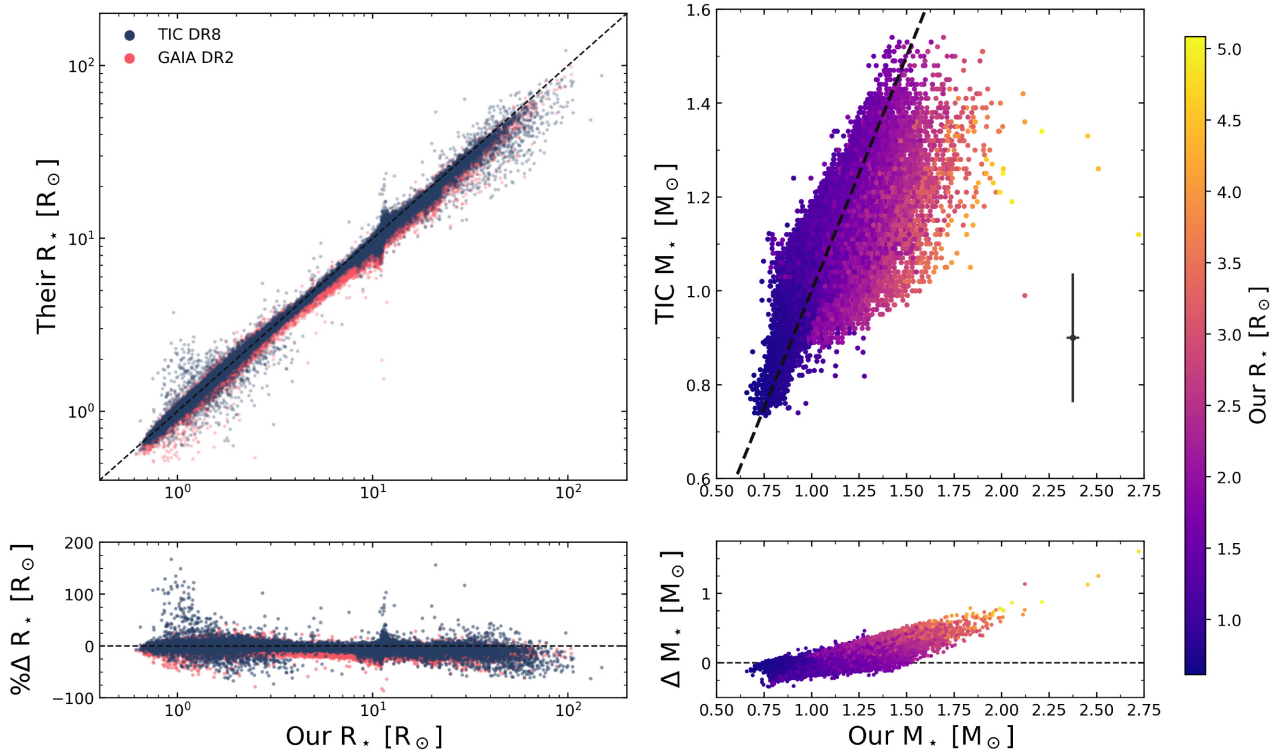
Figure 5. Left: Comparing the stellar radii of GALAH–*TESS* stars with the TIC (blue) and *Gaia* (pink). There is good overall agreement between the derived radius values, with a relative rms of 10 per cent and 14 per cent for *Gaia* DR2 and TIC values, respectively. An equality line is present in both plots, in the form of the dark grey dashed line. Right: Comparing our GALAH–*TESS* stellar masses with TIC-derived stellar masses. There is a good overall agreement between the derived `isochrone` masses and the TICs, with an rms of 0.12 $M_\odot$. Only dwarf stars within the TIC have mass measurements, and thus these comparisons are only valid for this luminosity class. Each star is coloured by its stellar radius, with median error bars given in the bottom-right corner.
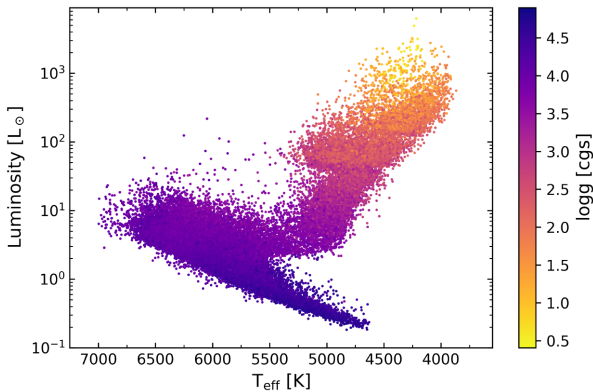
Figure 6. A Hertzsprung–Russell diagram of our GALAH–*TESS* catalogued stars using GALAH DR2's T_{eff} and our isochrone-derived luminosity values. Stars selected for our catalogue include both those on the main-sequence (lower right to mid-left; high log *g*) and evolved stars (mid-left to upper left; low log *g*). We have included giant stars within our catalogue as these stars are also known to host exoplanets, and it seems likely that analysis of *TESS*'s full-frame images will yield a number of new discoveries of this type.

## 3.2 Chemical abundances of GALAH–*TESS* stars

Our catalogue of ∼47 000 stars provides elemental abundances for up to 23 unique species derived from GALAH DR2 abundances. It is not possible, however, to provide accurate elemental abundances for all 23 elements for all of our target stars – and so we have only provided abundances for those species which can be reliably determined from each star's spectrum. As a result, 90 per cent of our sample have reliable O, Si, Mg, Si, Zn, and Y abundances, whilst just 2 per cent of the stars cataloged yield reliable Co abundances. In the most extreme case, only 23 stars in our catalogue have reliable, measured Li abundances. The median abundance values, along with the number of stars of which we have a particular abundance value for, can be found in Table 1. Generally, our catalogue median values are near Solar, with C, O, Al, K, and Fe median values being significantly sub-Solar, and Li, Co, Y, and La being significantly super-Solar (though Li suffers from small number statistics). Our distribution between selected elements and the measured Fe abundance is shown in Fig. 7. Given the paucity of Li measurements, we do not discuss the abundances of that element further in this work.[6]

To validate our stellar abundances, we made use of the online, interactive stellar abundance catalogue, the Hypatia Catalog Hinkel & Burger (2017a). The Hypatia Catalog is an amalgamation of stellar abundances, including physical and planetary parameters, for stars within 150 pc of the Sun (Hinkel et al. 2014, 2016; Hinkel & Burger 2017b). Comprised of mostly FGKM-type stars, the catalogue is compiled from more than 190 literature sources that can be normalized by several Solar normalizations, particularly Lodders et al. (2009). By using the Hypatia Catalog alongside the abundances within our sample, we can directly compare our abundances that use the same Solar normalization. We accessed the Hypatia Catalog on

---

[6]We direct the interested reader to Martell et al. (2020), and references therein, for a discussion of Li abundances from GALAH data, with a particular focus on the mechanisms by which different populations of stars can end up with dramatically different Li distributions.
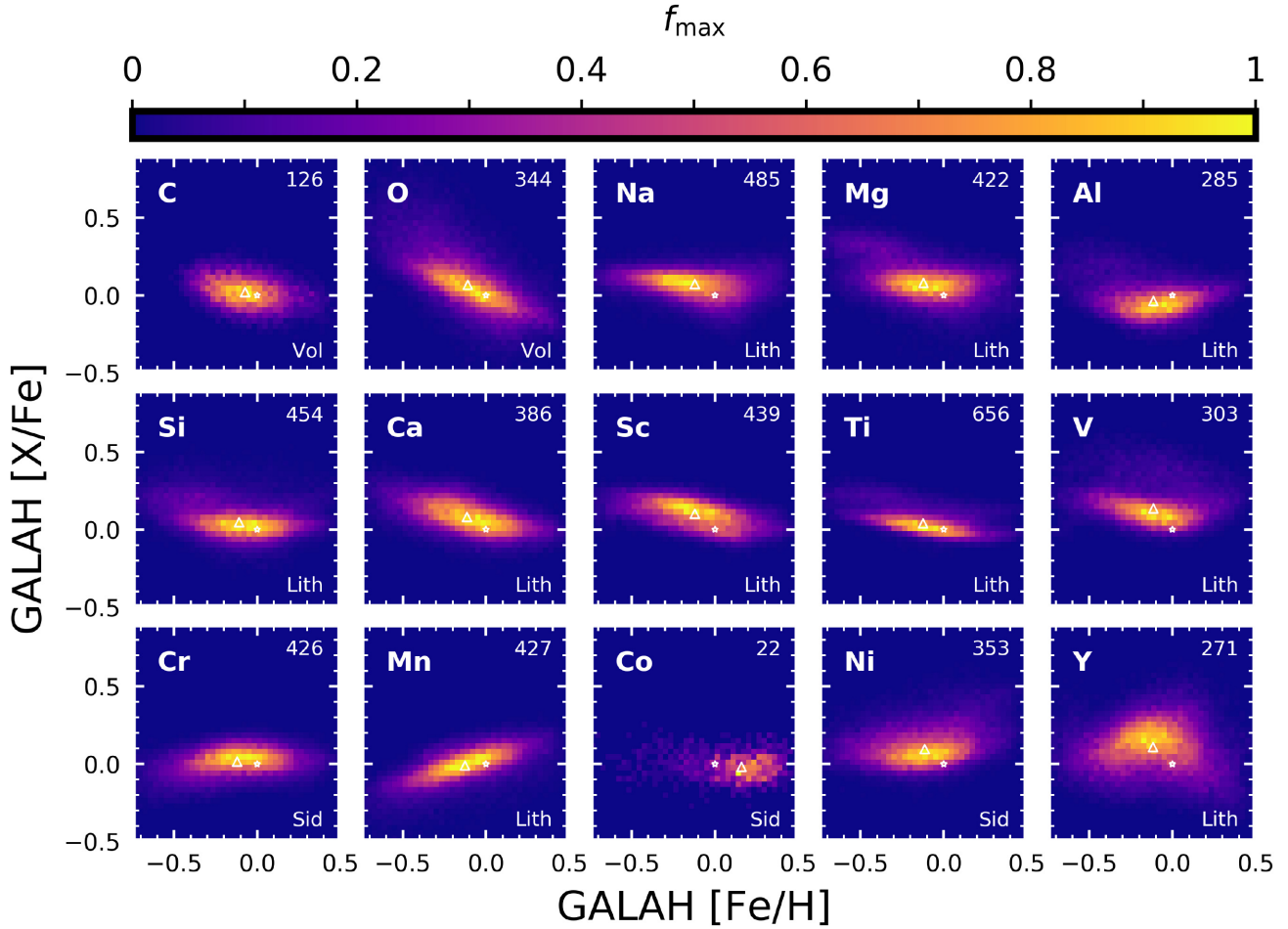
Figure 7. 2D histogram distributions of elemental abundances versus iron abundance for planet-building lithophile (Lith), siderophile (Sid), and volatile (Vol) elements. The Sun's values are represented on each plot by a white-bordered, hollow star, with the median values depicted by triangles. Since there are some elements that are easier to detect in a stellar photosphere than others, each bin is coloured by the fraction of the maximum bin value in each plot. The maximum bin value for each plot is given in the plot's top right-hand corner.

2020 August 6 and cross-matched our GALAH–*TESS* stars with stars within Hypatia by directly comparing their 2MASS identifiers.

Our GALAH–*TESS* catalogue contains data for 606 stars that are within 150 pc of the Sun, of which five matched with the Hypatia Catalog. Fig. 8 shows the comparison of elemental abundances for the five cross-matched stars, namely HD 121004, HD 138799, HD 139536, HD 89920, and HD 103197. HD 121004 is the only metal-poor star within our sample that was cross-matched with Hypatia, with the other four stars boasting super-Solar abundances. HD 121004, a G2V dwarf, has elemental abundances that show the best agreement with the abundances within Hypatia, with a median difference of 0.03 dex with those nine specific elements. The four iron-rich stars, which are all K dwarfs, show a minor discrepancy between their elemental abundances, with the GALAH abundances being enriched by 0.12–0.14 dex compared to Hypatia.

In terms of the abundance difference per element between our data and those presented in the Hypatia catalogue, the Ti abundances agree to within a median value of 0.03 dex, which is within the median 1σ error of GALAH–*TESS* and Hypatia Ti abundances for this sample, being 0.03 and 0.05 dex, respectively. The values for Ca, Al, and Na between the two catalogues differ by 0.08 dex, with the Fe, O, Si, Mg, and Ni abundances varying between the catalogues by between 0.12 and 0.16 dex. The GALAH DR2 abundances include non-Local

Thermodynamic Equilibrium (non-LTE) effects for O (Amarsi et al. 2016a), Na, Mg (Osorio et al. 2015; Osorio & Barklem 2016), Al, Si (Amarsi & Asplund 2017), and Fe (Amarsi et al. 2016b) (Buder et al. 2018; Gao et al. 2018), whereas the Hypatia abundances (from Adibekyan et al. 2012) do not take into account non-LTE affects, which may explain the discrepancy between the difference in elemental abundance values.

We calculated the Mg/Si, Fe/Mg, Fe/Mg, and C/O abundance ratios using our GALAH–*TESS* [X/H] values and Solar values from Lodders et al. (2009). We only returned a ratio value if stars had both elements available to us, with 43 162 Fe/Si, 44 968 Fe/Mg, 41 741 Mg/Si, and 9521 C/O abundance measurements available. The limited C/O ratio measurements reflect the one atomic C line and two O lines available for reliable abundance measurements across HERMES' wavelength coverage and resulting detection limits. The median and 1σ error values for our selected GALAH–*TESS* abundance ratios are presented in Table 2. For reference, the Solar values for Fe/Si, Fe/Mg, Mg/Si, and C/O using Lodders et al. (2009) are 0.85, 0.81, 1.05, and 0.46, respectively.[7] Our abundance ratios all tend to have sub-Solar Fe/Si, Fe/Mg, Mg/Si, and C/O ratios. The

---

[7]Solar abundance ratios are calculated by $\log_{10}(X/Y)_{\odot} = A(X)_{\odot} - A(Y)_{\odot}$.
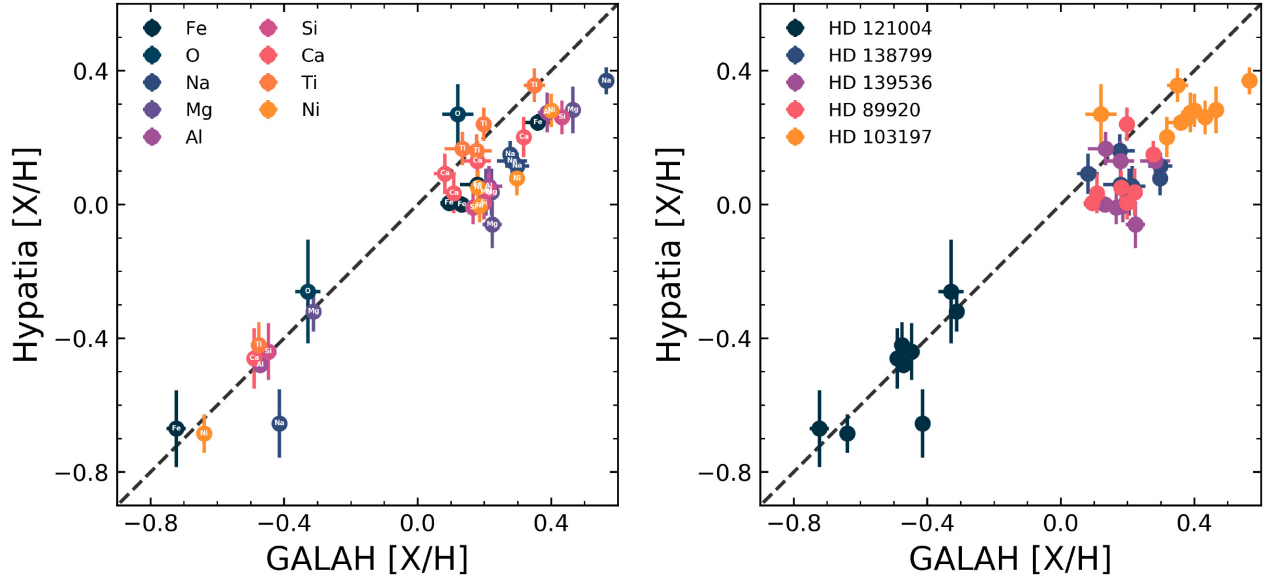
Figure 8. Both of these plots compare the elemental abundances for nine different elements across five stars cross-matched with the Hypatia Catalog (Hinkel & Burger 2017a). Left: Comparing by element with each element given a unique colour identifier. Right: Same plot as the left; however, abundances are now grouped by star, labeled by their Henry Draper catalogue (HD) identifier.

Table 1. Here, we present the median and 1σ error values for [X/H] abundances derived in our GALAH–*TESS* catalogue normalized by Lodders et al. (2009). We also give the number of stars in our catalogue for which a reliable value for the abundance in question was obtained. The 1σ error values here quoted are the median 1σ error values for each elemental abundance. The paucity of stars with a reliable Li abundance is particularly apparent.

X	Number of stars	[X/H] (dex)	X	Number of stars	[X/H] (dex)
Li	28	2.02 ± 0.06	Cr	38771	-0.07 ± 0.04
C	9716	-0.16 ± 0.07	Mn	39214	-0.07 ± 0.04
O	43297	-0.15 ± 0.07	Fe	47289	-0.12 ± 0.07
Na	44762	0.13 ± 0.05	Co	1057	0.14 ± 0.05
Mg	44972	-0.05 ± 0.03	Ni	39450	-0.00 ± 0.03
Al	24068	-0.14 ± 0.06	Cu	22598	0.04 ± 0.04
Si	43164	0.00 ± 0.01	Zn	43976	0.09 ± 0.02
K	34258	-0.29 ± 0.06	Y	43490	0.33 ± 0.04
Ca	41491	-0.06 ± 0.05	Ba	28751	0.02 ± 0.06
Sc	41641	-0.04 ± 0.05	La	8522	0.17 ± 0.05
Ti	39205	-0.07 ± 0.06	Eu	5799	-0.06 ± 0.05
V	27403	0.09 ± 0.04	–	–	–

Table 2. Median and 1σ error values for our GALAH–*TESS* abundance ratios. The majority of our stars have Mg/Si, Fe/Mg, and Fe/Mg values; however, only 20 per cent have reliable C/O measurements.

|	Number of stars	(X/Y)	(X/Y)$_\odot^a$
Fe/Si	43162	0.65 ± 0.22	0.85
Fe/Mg	44968	0.68 ± 0.23	0.81
Mg/Si	41741	0.98 ± 0.22	1.05
C/O	9521	0.44 ± 0.13	0.65

^{a}Solar values from Lodders et al. (2009).

distribution of our C/O and Mg/Si values are plotted against each other in Fig. 13, and are discussed in more detail in Section 4.2.

Stellar elemental abundances can change slightly, depending upon the Solar normalization used to derive such abundances. To illustrate this, we have then created Fig. 9 to show the distribution of our [X/H] abundances for planet-building elements scaled to the various Solar normalizations that are widely used within exoplanetary science. These rocky-planet building elements include the volatiles, which typically reside in the atmosphere (C, O), the lithophiles, which are present in the crust/mantle of rocky planets (Na, Mg, Al, Si, Ca, Sc, Ti, V, Mn, Y), and the siderophiles, which easily alloy with Fe and primarily reside in the core (Cr, Fe, Co, Ni) (Hinkel et al. 2019). Having six different normalizations means that each star in the sample is counted six times. However, this allows the skewed distributions from the different methods to be assessed in a single figure, and forms the basis for Fig. 9, where we present the skews for all sixteen planet-building elements.

From Fig. 9, it is readily apparent that there is general overall agreement among our abundances normalized by Lodders et al. (2009), when compared to other distributions with the total median of the distributions falling within 1σ of our L09 values. Volatile elements such as C and O and lithophiles Na and Mg tend to negative [X/H] values in older normalizations compared to newer normalizations that instead peak towards super-Solar values. We have incorporated Fig. 9 into this work to show the exoplanetary community the importance of referencing what Solar normalizations are used within their work, as abundance values will differ depending upon these normalizations. Larger changes can be seen in the spread of median C/O, Mg/Si, and Fe/Mg abundance ratios for these different Solar normalizations. The spread of our median C/O values vary from 0.44 to 0.64, from 0.98 to 1.35 for Mg/Si, and from 0.58 to 1.39 for Fe/Mg depending upon what Solar normalization is used. Changing the value of Mg/Si for a given planet would have the primary effect of altering the mantle mineralogy between olivine rich and pyroxene rich (Hinkel & Unterborn 2018; Unterborn & Panero 2017; Brewer & Fischer 2016; Thiabaud et al. 2014a, 2015). These differences in composition are known to change the degree of melting and crustal composition (Brugman, Phillips & Till 2020), but the degree that that composition changes the interior behaviour of a rocky exoplanet remains an area of active research. These results therefore highlight the importance of normalizing abundances to the same Solar normalizations when comparing chemical abundances
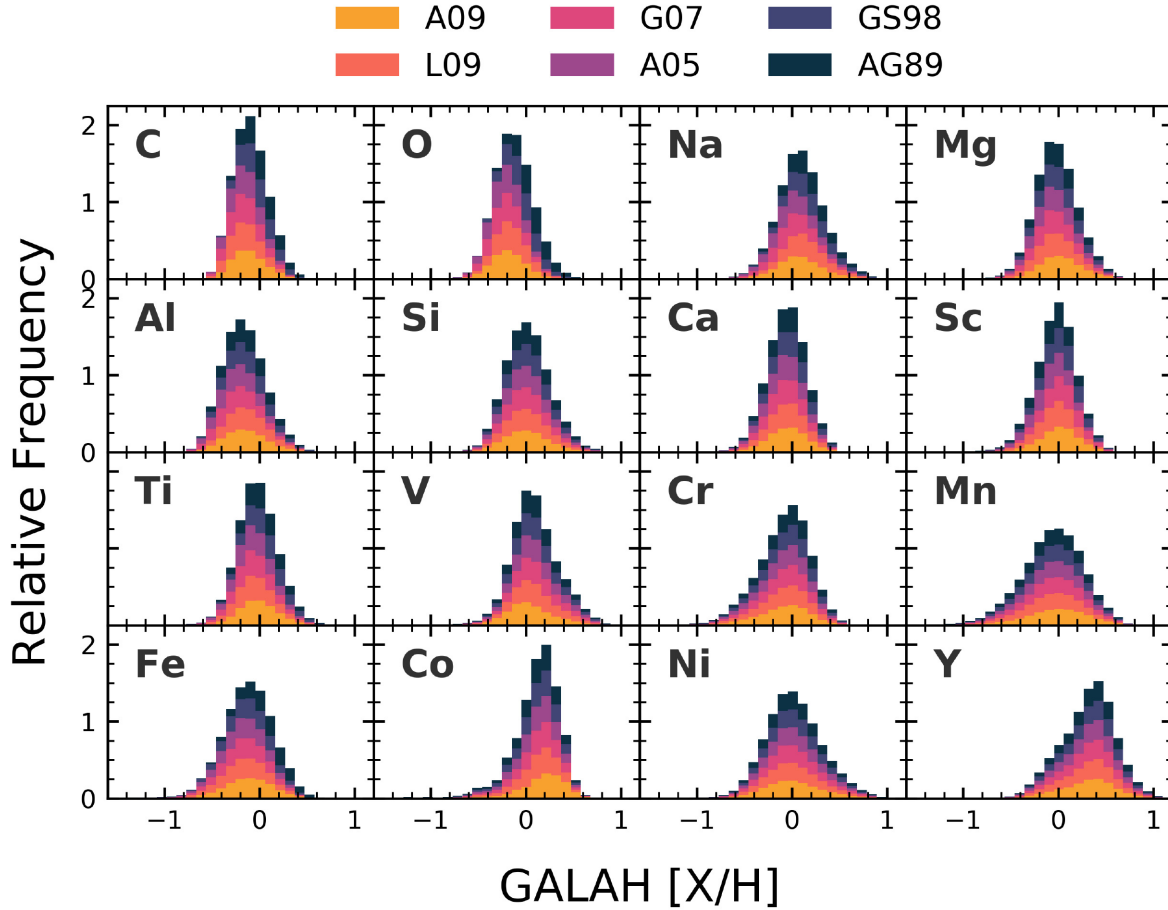
Figure 9. The same distribution of planet-building elements as found in Fig. 7. Here, however, we have normalized our [X/H] values to various Solar normalizations including Asplund et al. (2009), Lodders et al. (2009), Grevesse, Asplund & Sauval (2007), Asplund, Grevesse & Sauval (2005), Grevesse & Sauval (1998), and Anders & Grevesse (1989), displayed in yellow, orange, pink, purple, violet, and navy, respectively. Combining the stellar abundances in this manner with different Solar normalizations shows the general trends within a certain element, unbiased by using a specific Solar normalization.

from different surveys and considering the implications those results might have on inferring the structure of rocky exoplanets.

4 DISCUSSION

In this section, we discuss the refinement of planetary systems with the newly derived GALAH–*TESS* stellar parameters (Section 4.1) and how the X/Y molar abundance ratios of stars within GALAH–*TESS* can inform us in forward predicting what possible planetary systems and makeups these stars may host (Section 4.2).

4.1 Refining planetary system parameters

Within our GALAH–*TESS* sample, we cross-matched our GALAH–*TESS* sample with the catalogue of known planetary systems on NASA's Exoplanet Archive and TOIs or CTOIs by accessing the Exoplanet Follow-up Observing Program for *TESS* (ExOFOP–TESS)[8] website. At the time of writing, the GALAH–*TESS* catalogue contains three confirmed single-planet systems: WASP-61 (Smith et al. 2012), WASP-182 (Nielsen et al. 2019a), and HD 103197 (Mordasini et al. 2011). Our catalogue also includes five single-planet candidate systems namely TOI-745, TOI-815, TOI-1031, TOI-777,

and TOI-1126. We should note that WASP-61b is also known as TOI 439.01. Lastly, there are also three CTOI planetary systems, two of which host two candidates, TIC 201256771 and TIC 220402290. The other CTOI system is a three-planet candidate system, TIC 300903537. A brief summary of the revised stellar parameters for these 11 confirmed and candidate exoplanet hosts are summarized in Table 3.

The calculated radius of an exoplanet is directly related to the radius of its host star – so any change in stellar radius will change the radius of the planet. All of our exoplanets and candidates have transit depth measurements from *TESS*, which we obtain from ExOFOP-TESS, except for WASP-182b and HD 103197b. For the short-period transiting exoplanet WASP-182b, there is currently no transit data from *TESS*. Instead, we use the transit depth values from its discovery paper (Nielsen et al. 2019a) to refine its radius. Unfortunately, at the time of writing, the longer-period exoplanet HD 103197b has not been observed to transit its host, and no direct size determination is possible.

A brief summary of the revised planetary radii for the 14 confirmed and candidate exoplanets are summarized in Table 4 along with the transit depth and literature planetary radii against which we are able to compare our results.

By far the most surprising result from our refinement of planetary radii is the refinements of two planetary candidates orbiting the

Table 3. Our stellar physical parameters of matched confirmed and candidate exoplanet hosts. For CTOI hosts, since their CTOI ID is simply their TIC ID, we have omitted this column from the table. [M/H] in this table is the overall metallicity and not the host star's iron abundance, [Fe/H].

Catalogue ID	TOI ID	TIC ID	$T_{\rm eff}$ (K)	[M/H] (dex)	$\log g$ (cgs)	$M_\star$ ($M_\odot$)	$R_\star$ ($R_\odot$)
WASP-61	439	13021029	6245 ± 58	-0.06 ± 0.08	4.03 ± 0.17	1.20 ± 0.03	1.38 ± 0.02
UCAC4 238-060232	754	72985822	6096 ± 59	0.13 ± 0.08	4.16 ± 0.17	1.16 ± 0.04	1.21 ± 0.03
CD-43 6219	815	102840239	4954 ± 34	0.13 ± 0.05	4.46 ± 0.11	0.83 ± 0.01	0.76 ± 0.01
UNSW-V 320	–	201256771	4979 ± 50	0.04 ± 0.07	3.42 ± 0.15	1.29 ± 0.09	3.22 ± 0.07
CD-57 956	–	220402290	5817 ± 41	0.08 ± 0.06	4.33 ± 0.13	1.04 ± 0.03	1.10 ± 0.01
UCAC4 306-282520	–	300903537	4841 ± 83	0.2 ± 0.09	4.41 ± 0.19	0.82 ± 0.02	0.80 ± 0.01
HD 81655	1031	304021498	6415 ± 44	-0.19 ± 0.06	3.88 ± 0.14	1.32 ± 0.04	1.89 ± 0.02
HD 106100	777	334305570	6187 ± 35	0.12 ± 0.05	3.82 ± 0.11	1.28 ± 0.02	1.54 ± 0.02
WASP-182	–	369455629	5615 ± 50	0.32 ± 0.07	4.15 ± 0.15	1.05 ± 0.03	1.25 ± 0.02
HD 103197	–	400806831	5223 ± 32	0.35 ± 0.04	4.43 ± 0.11	0.94 ± 0.02	0.90 ± 0.01
TYC 7914-01572-1	1126	405862830	5108 ± 55	0.09 ± 0.08	4.66 ± 0.17	0.82 ± 0.02	0.74 ± 0.01

Table 4. Our refined planetary radii values for confirmed and TESS candidate exoplanets. All literature radius values and transit depth values come from ExOFOP-TESS except for WASP-182b, where its literature planetary radius and transit depth values are from Nielsen et al. (2019a). We have flagged problematic planetary candidates in bold. From our revised planetary radii, CTOI 201256771.01 and CTOI 201256771.02 now have radii comparable to the Sun, and thus are not exoplanets. The orbital periods of CTOI 220402290.01, CTOI 220402290.02, CTOI 300903537.01, and CTOI 300903537.02 are problematic and are likely duplications of the same event. This is discussed further in Section 4.1. Since some of these planet candidates are comparable in scale to that of Jupiter, the conversion between Jupiter's radius to Earth's is $R_J = 11.209\,R_\oplus$.

TOI/CTOI ID	TIC ID	ΔF (mmag)	Our R_p ($R_\oplus$)	Literature R_p ($R_\oplus$)
439.01	13021029	9.04283 ± 0.00143	13.68 ± 0.20	13.27 ± 0.47
754.01	72985822	8.93564 ± 0.50239	12.00 ± 0.48	13.90 ± 13.91
815.01	102840239	1.25 ± 0.00155	2.81 ± 0.13	2.87 ± 0.13
201256771.01	**201256771**	**84.34287 ± 8.98023**	**96.17 ± 5.34**	**24.72**
201256771.02	**201256771**	**97.59384 ± 10.39110**	**103.15 ± 5.69**	**26.51**
220402290.01	**220402290**	**21.84594 ± 2.32600**	**17.02 ± 0.93**	**17.15**
220402290.02	**220402290**	**44.09427 ± 4.69485**	**24.05 ± 1.30**	**24.25**
300903537.01	**300903537**	**94.16304 ± 10.02582**	**25.06 ± 1.33**	**25.10**
300903537.02	**300903537**	**11.02043 ± 1.17338**	**8.74 ± 0.48**	**8.75**
300903537.03	300903537	3.74782 ± 0.39904	5.10 ± 0.28	5.11
1031.01	304021498	1.18 ± 0.00172	6.80 ± 0.08	6.91 ± 0.46
777.01	334305570	2.80673 ± 0.08351	8.56 ± 0.16	7.32 ± 1.15
WASP-182 b	369455629	0.01067 ± 0.00000	8.90 ± 0.15	9.53 ± 0.34
1126.01	405862830	1.06 ± 0.00144	2.53 ± 0.02	2.62 ± 0.11

star TIC 201256771. Currently, TIC 201256771 hosts two CTOIs, 201256771.01 and 201256771.02, which are recorded on ExOFOP–TESS as having radii of $24.72\,R_\oplus$ and $26.51\,R_\oplus$, respectively. With our revised radii, these candidate events observed in TESS Sector 1 now have radii comparable with stellar radii (Chen & Kipping 2017) of $96.17 \pm 5.34\,R_\oplus$ and $103.15 \pm 5.69\,R_\oplus$, respectively. This casts serious doubts about the planetary nature of these candidate events, especially with their orbital periods being only separated by 17 min, with the orbital periods of CTOI-201256771.01 and CTOI-201256771.02's being stated as 3.754861 and 3.766667 d, respectively. Upon further investigation, this system is a known eclipsing binary that has an orbital period nearly equal to the candidates, being 3.76170 d (Christiansen et al. 2008). From this data alone, we conclude that CTOI 201256771.01 and CTOI 201256771.01 are candidates of the same event, being the transit of the eclipsing companion to UNSW-V 320. Apart from this extreme example, the rest of our planetary radii fall nicely within the current literature values and their uncertainties, all of which can be found in Table 4. Upon the revision of this CTOI system, we re-checked the sensibility of the other CTOI systems within our planet-host sample. The orbital periods of CTOI 220402290.01 and CTOI 220402290.02 are 0.7833 and 0.7222 d, respectively, or roughly 90 min. This would mean that

their orbital separation would be comparable to their radii, which deems this system as extremely unstable. These transit events are likely caused by a single candidate, rather than two. Similarly, the orbital periods of CTOI 300903537.01 and CTOI 300903537.02 only differ by 36 min and are likely caused by the same candidate.

Of our known confirmed and candidate exoplanets, only three have measured mass values. The most conventional way that an exoplanet's mass is determined is through the radial velocity technique. Specifically, an exoplanet's line-of-sight mass, $M_p \sin i$ is determined through measurement of the semi-amplitude of the host's radial velocities measurement, K_{RV}, orbital eccentricity, e, period P, and stellar mass $M_\odot$ (Lovis & Fischer 2010). If the orbital inclination, i, of the system is known, traditionally found through fitting models to the photometric transit curve, we can then calculate the planet's true mass, M_p.

We use literature values for these planetary systems, namely WASP-182b values from Nielsen et al. (2019a) as well as WASP-61b and HD 103197b values from Stassun, Collins & Gaudi (2017). We combine these with the masses of their host stars in order to revise the planetary mass of the exoplanets. Our revised planetary mass values, along with the previous literature values, can be found in Table 5. As with the refined radii results, there is excellent overall

Table 5. With our newly derived stellar mass values, we have refined the mass of three exoplanets, WASP-61 b, WASP-182b, and HD 103197 b. In this table, we have used our new stellar mass values, along with literature semi-amplitude (K) and orbital eccentricity (e), period (P), and inclination (i) values to derive the new planetary mass values.

Planet Name	TIC ID	K_{RV} (ms^{-1})	P (d)	e	i (deg)	Our M_p ($M_\oplus$)	Literature M_p ($M_\oplus$)
WASP-61 b	13021029	233 ± 0	3.8559 ± 3.00e-06	0	89.35 ± 0.56	646.01 ± 9.82	851.784 ± 266.977
WASP-182 b	369455629	19 ± 1.2	3.376985 ± 2.00e-06	0	83.88 ± 0.33	46.41 ± 3.05	47.039 ± 3.496
HD 103197 b	400806831	5.9 ± 0.3	47.84 ± 0.03	0	–	32.06 ± 1.67*	28.605 ± 6.357*

Note. Literature values for WASP-182b come from Nielsen et al. (2019a) and WASP-61b and HD 103197b's values are from Stassun et al. (2017). Asterisk (∗) denotes that HD 103187b's mass is actually $M_p \sin i$ in this current form, as there is yet to be any inclination data retrieved from this particular planetary system. Since some of these exoplanets are comparable in scale to that of Jupiter, the conversion between Jupiter's mass to Earth's is $M_J = 317.83\ M_\oplus$.

agreement with our mass values compared to the literature. All three refined planetary mass values fall within 1σ error bars of the previous literature values. The biggest increase of planetary mass precision with our results comes from the Jovian type exoplanet HD 103197 b. We have refined the mass of HD 103197b from a percentage error of 31 per cent down to 2 per cent, thanks largely due to the refinement in the stellar mass of HD 103197.

Overall, our refined planetary mass and radius results are in good agreement with their literature values. This also validates the overall good agreement with our refined stellar mass and radius values. Even though the change in planetary mass or radius of 10–20 per cent might intuitively be insignificant in re-characterizing Jovian worlds, it does however have larger implications for smaller planets like our own.

For example if an Earth-like planet in mass and radius (1.0R$_\oplus$,1.0M$_\oplus$), characterized by the TIC, was discovered orbiting around any of our GALAH–*TESS* stars, would this planet still be 'Earth-like' with our revised stellar parameters? Using a similar approach to that of Johns et al. (2018), we can refine the planetary radius and mass of this fictitious Earth using both GALAH-*TESS* and TIC catalogue values of stellar and planetary mass and radius values.

Our refined radius and mass values for these fictitious Earth-like exoplanets are displayed in Fig. 10. Roughly 85 per cent of our planets fall within ±10 per cent of Earth-like mass and radius values. Beyond this ±10 per cent, there is a wide variety of mass and radius values throughout the plot, which would suggest that these exoplanets that were once thought to be Earth-like, are now anything but. From Fig. 10, there are varying degrees of bulk composition for these 'Earth-like' worlds. In extreme cases, a putative 'Earth-like' planet's bulk density varies between a scaled-up Enceladus-like world (i.e. dominated by layers of water and a silicate core) (Schubert et al. 2007; Zolotov et al. 2011), to a possible remnant Jovian-world core dominated by iron (Benz et al. 2007; Mocquet, Grasset & Sotin 2014) with the habitability of such worlds still up for debate (Noack, Snellen & Rauer 2017; Kite & Ford 2018; Lingam & Loeb 2019). This shows that not only do we need better precision for stellar masses and radii, which better constrain the planetary mass and radius values, but there also needs to be a level of consistency across these fundamental parameters for future follow-up characterization.

There are already a wide variety of planetary radius and mass values for known super-Earth and Earth-sized worlds and thus there will be a wide variety of planetary compositions. A fundamental problem with inferring planetary compositions through mass–radius or ternary/quaternary diagrams (Rogers & Seager 2010; Brugger et al. 2017) is that they cannot uniquely predict the interior composition of a given exoplanet. A variety of different interior compositions can lead to identical mass and radius values (Dorn et al. 2015; Unterborn et al. 2016; Suissa et al. 2018; Unterborn & Panero 2019). This gives

rise to an inherent density degeneracy problem. A wide variety of planetary compositions are allowed, especially if the models used have three or more layers. This is typical for most that assume a three (core, mantle, ocean) or four-layered planet (core, mantle, ocean, atmosphere). Current Bayesian inference (Dorn et al. 2015) and forward models (Unterborn et al. 2018a; Unterborn, Desch & Panero 2018b) break down this degeneracy, using stellar abundance ratios to infer an exoplanet's composition. These abundance ratios and their importance are described in Section 4.2.

4.2 Importance of stellar abundances to exoplanetary science

Within our own Solar system, observations show that the relative abundances of refractory elements such as Fe, Mg, and Si, elements crucial in forming rocky material for planets like ours to build upon, are similar within the Sun, Earth, Moon, and Mars (Wang et al. 2019b; Lodders 2003; McDonough & Sun 1995; Wanke & Dreibus 1994). The bulk planetary and stellar ratios of these elements during planetary formation are also similar, suggesting that stellar Fe/Mg and Mg/Si can assist with determining the building blocks of the planets they host (Bond et al. 2010b; Thiabaud et al. 2015, 2014a). These elemental abundances can help us understand what elements favour certain planetary architectures and can also provide constraints on the internal geological composition of exoplanets (Brugger et al. 2017; Dorn et al., 2015, 2017a; Unterborn et al. 2018a).

In particular, the elemental abundance ratios of Mg/Si, Fe/Mg, and C/O are fundamental for probing the mineralogy and structure of rocky exoplanets. The formation, structure, and composition of exoplanets is extremely complex, with these generalizations not taking into account planetary migration or secondary processes such as giant impacts. A more comprehensive analysis of GALAH DR2's abundances trends, galactic populations and implications for planet-building elements can be found in Bitsch & Battistini (2020) and Carrillo et al. (2020).

4.2.1 Estimating the size of a rocky planet's core through stellar Fe/Si ratios

The amount of mass contained within a rocky exoplanet's core is determined by its Fe/Si ratio (Brugger et al. 2017; Dorn et al. 2015; Unterborn et al. 2018a). An increasing Fe/Si ratio would result in a larger core mass fraction compared to a larger mantle core fraction for smaller values of Fe/Si. Within our Solar system, Earth (McDonough 2003; McDonough & Sun 1995), and Mars (Wanke & Dreibus 1994) have comparable bulk Fe/Si values to that of photospheric Solar values (Lodders et al. 2009; Lodders 2003). Mercury, however, is an anomaly with its bulk Fe/Si value estimates ranging from ∼5 to 10,
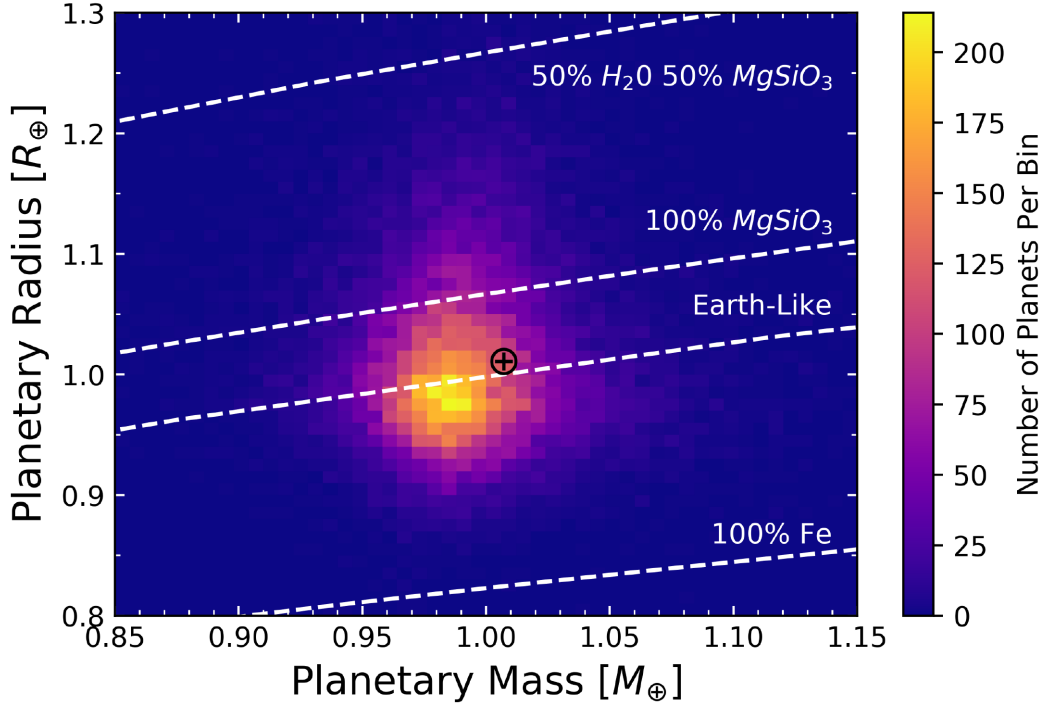
Figure 10. Simulation for the effects of parameter refinement on the mass and radius for a fictitious Earth-like planet discovered using the TIC catalogue. The mass–radius relationships used for the dashed lines to show density curves for a 50 per cent water-50 per cent rocky, pure rocky (containing pure post-perovskite $MgSiO_3$), 'Earth-like' (33 per cent Fe and 67 per cent rock) and pure iron worlds are from (Zeng, Sasselov & Jacobsen 2016). The black symbol '$\oplus$' represents the Earth's mass and radius. In extreme cases, a putative 'Earth-like' planet varies between a scaled-up Enceladus-like world (i.e. dominated by layers of water and a silicate core), to a Fe-enriched, Mercury-like planet. This simulation shows the need for consistency and precision in exoplanetary mass and radius determination for meaningful comparative planetology.

corresponding to a core mass fraction of ~45–75 per cent compared to a Fe/Si ratio near ~1.00 and a core mass fraction of 32 per cent for Earth (Nittler et al. 2017; Brugger et al. 2018; Wang et al. 2019b).

It is possible for the majority of iron to be contained within silicate material including bridgmanite ($MgSiO_3$/$FeSiO_3$), magnesiowüstite (MgO/FeO), olivine (Mg_2SiO_4/Fe_2SiO_4), and pyroxenes ($Mg_2Si_2O_6$/$Fe_2Si_2O_6$) for bulk Fe/Si values less than 1.13 (Alibert 2014). For Fe/Si > 1.13, models suggest that an iron core needs to be present within a rocky exoplanet to explain such a high ratio. This limit is calculated by simple stoichiometry and may not reflect the actual distribution of iron throughout a rocky exoplanet's core and mantle. The oxygen fugacity can also affect the distribution of a planet's iron distribution (Bitsch & Battistini 2020), oxidizing with mantle constituents instead of being differentiated into a core if the oxygen fugacity is too high (Elkins-Tanton & Seager 2008). This would result in a lower core mass fraction compared to situations of lower fugacity. Current models show that iron can be taken up in the mantle (Dorn et al. 2015; Unterborn et al. 2018a) as well as silicon being taken up within an iron core (Hirose, Labrosse & Hernlund 2013). Thus, Fe/Mg is a better proxy for core-to-mantle ratio and is produced within the GALAH–*TESS* catalogue.

Fig. 11 shows the distribution of Fe, Mg, and Si for our sample of GALAH–*TESS* stars. We can calculate the core mass fraction of potential rocky planets hosted by GALAH-*TESS* stars, using stiochiometry by the equation:

$$CMF = \frac{\#Fe\mu_{Fe}}{\#Mg(\mu_{Mg} + \mu_O) + \#Si(\mu_{Si} + 2\mu_O) + \#Fe\mu_{Fe}} \quad (3)$$

where $\#X$ represents the molar abundance of element X and μ_X is the molar weight of that element. We are able to use this estimation as

Fe, Mg, and Si all have similar condensation temperature (Lodders et al. 2009) and thus thermal processes are unlikely to fractionate the elements relative to each other. That is while a planet may have significantly fewer atoms of Fe and Mg than the host star, the Fe/Mg ratio of the star and planet may only be different by ~10 per cent (Bond et al. 2010a; Thiabaud et al. 2014b; Unterborn & Panero 2017). While mantle stripping by large impacts may increase the planet's Fe/Mg ratio (e.g. Bonomo et al. 2019), equation (3) represents a reasonable upper-bound for CMF for most systems. As mentioned above, changes in oxygen fugacity will convert some core Fe into mantle FeO, which will lower the CMF for a given bulk composition. From this ternary we can see that stellar abundances outline a wide range of CMF compared to the Earth and Sun, with their abundances falling near the middle of the distribution (Fig. 12). Less than 0.3 per cent of our stars have Fe/Si > 1.13 (Fig. 12); therefore, the rocky planets possibly orbiting GALAH-*TESS* stars may have their iron content distributed between both core and mantle layers with marginally lower CMF than predicted in Fig. 11.

4.2.2 Mantle compositions of rocky exoplanets through stellar host Mg/Si and C/O ratios

The structure and composition of super-Earths and sub-Neptunes can be constrained through theoretical models using their host's Mg/Si and C/O elemental ratios. The stellar C/O abundance chemically controls the silicon distribution amongst oxides and carbides (Bond et al. 2010b; Carter-Bond et al. 2012; Duffy, Madhusudhan & Lee 2015). For those stars with C/O values less than 0.8, Mg/Si controls the mantle chemistry by varying the relative proportions of olivine,
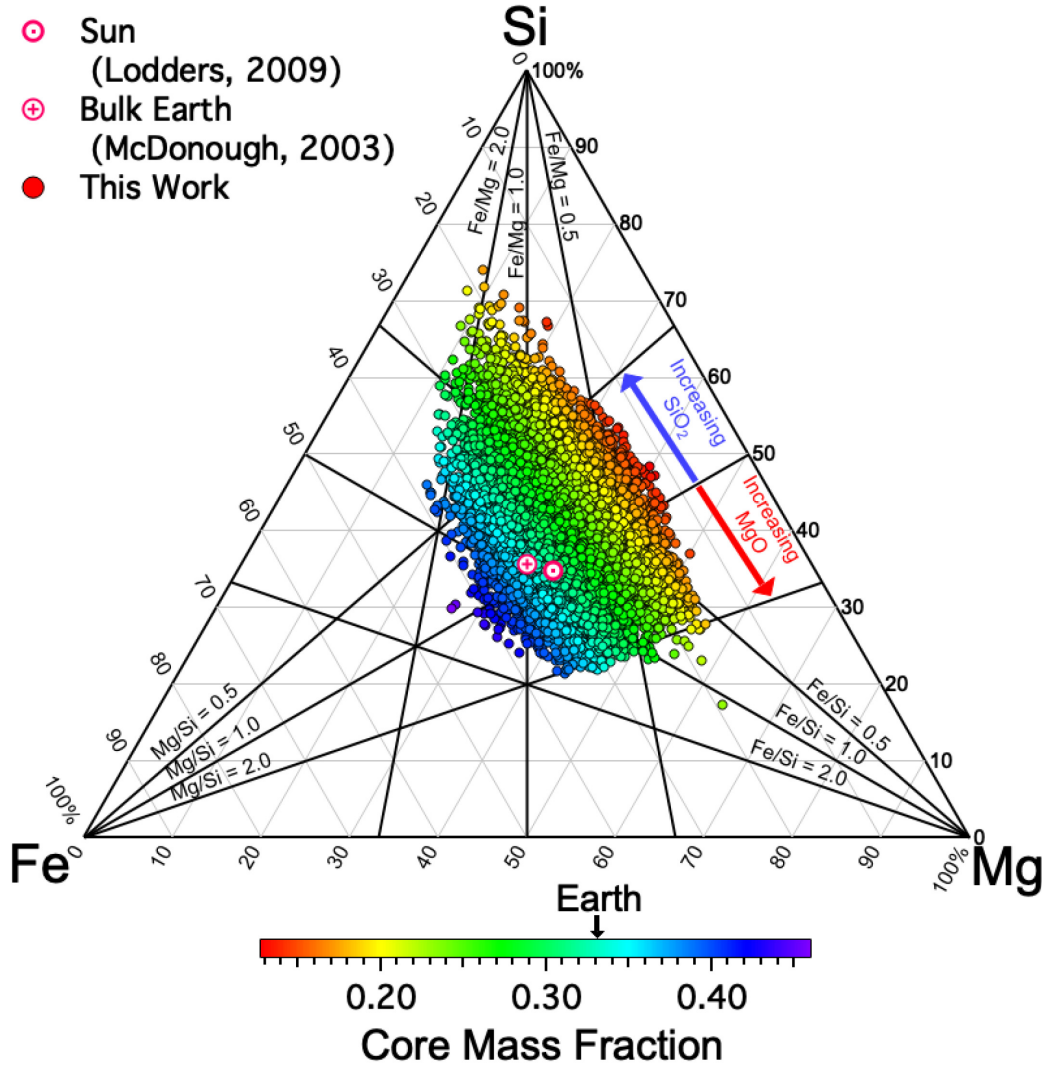
Figure 11. Ternary diagram of the Fe, Mg, and Si abundances from the for our GALAH–*TESS* stars, assuming a Solar abundance model of Lodders et al. (2009). In general, the closer to an individual corner of the ternary a data point falls the greater the proportion of that element in the resulting planet assuming stellar composition roughly reflects planetary composition (Bond et al. 2010a; Thiabaud et al. 2014b; Unterborn & Panero 2017). Individual points are colour coded to show the maximum core mass fraction (CMF) of the planet, assuming all Fe is present in the core and Mg and Si are in their oxide forms (MgO, SiO$_2$). The Earth (McDonough 2003) and Solar (Lodders et al. 2009) abundances are shown for reference.

pyroxenes and oxides. However, within this realm of low C/O values, there are two distinct regimes in which the Mg and Si are distributed within the mantle:

(i) In a 'silicon-rich' environment, whereby the Mg/Si < 1, the upper mantle will be dominated by ortho- and clino-pyroxene, majoritic garnet (Mg$_3$(MgSi)(SiO$_4$)$_3$) as well as SiO$_2$ (either as quartz or coesite) with the lower mantle consisting of bridgmanite ((Mg,Fe)SiO$_3$) and stishovite (SiO$_2$). As Mg/Si decreases, the proportion of stishovite will increase at the cost of brigmanite in the lower mantle.

(ii) For larger values of Mg/Si, where Mg/Si > 1, a rocky planet's upper mantle will mostly comprise of olivine (Mg$_2$SiO$_4$), pyroxenes and majoritic garnet, with bridgmanite and magnesiowüstite (or ferropericlase) ((Mg,Fe)O) in lower mantle. As the Mg/Si ratio increases, so does the amount of olivine and ferropericlase within the rocky planet's upper and lower mantle respectively. This regime of planetary composition is akin to rocky worlds (i.e. Mars and Earth) within our Solar system and thus labelled as 'terrestrial-like' mantle

compositions within our paper (Unterborn & Panero 2017; Duffy et al. 2015; Carter-Bond et al. 2012; Bond et al. 2010b). As Mg/Si increases, the proportion of magnesiowüstite will increase at the cost of brigmanite in the lower mantle.

However, these compositions only extend for C/O < 0.8. For C/O > 0.8, exotic mantle compositions of graphite and the carbides including SiC can start to dominate the geological composition of an exoplanet's core and mantle, when planets form within a protoplanetary disc's innermost region (Kuchner & Seager 2005; Carter-Bond et al. 2012; Unterborn et al. 2014; Wilson & Militzer 2014; Nisr et al. 2017; Miozzi et al. 2018;). These 'carbon-rich' worlds can extend out through carbon-rich discs and can even form with C/O ratios as low as 0.67 (Moriarty, Madhusudhan & Fischer 2014). However, the habitability of such worlds is still under debate, with some studies suggesting that habitability is unlikely. This is because theoretical models suggest that these worlds would likely be geodynamically inactive planets and would limit the amount of carbon-dioxide degassing into its atmosphere (Unterborn et al. 2014).
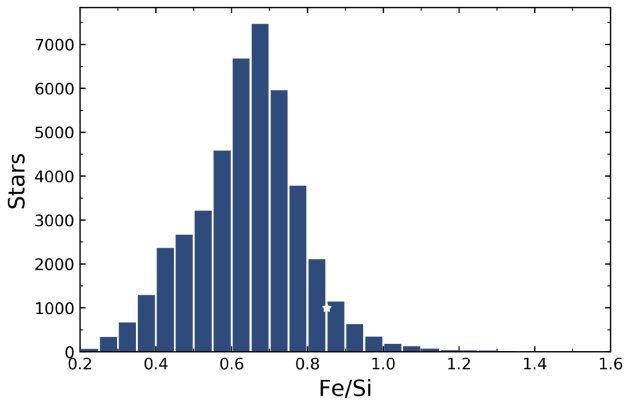
Figure 12. Of the 47 285 stars within our sample, only 134 have Fe/Si values greater than 1.13 which would indicate the vast majority of our possible rocky worlds will have their iron content distributed between their iron and mantle layers. An iron-core must be present beyond Fe/Si values of 1.13 to explain such a high Fe/Si ratio. The white star within the histogram depicts the Sun's photospheric Fe/Si value of 0.85 (Lodders et al. 2009).

Our C/O and Mg/Si distribution for the GALAH–*TESS* stars are found in Fig. 13. Of our 47 000+ sample, only 8832 stars have C/O and Mg/Si ratios as most stars' C or O abundances were flagged by *The Cannon*. This sample also includes exoplanet host WASP-61 and candidate hosts UCAC4 238-060232 (TOI-754) and HD 81655 (TOI-1031). A total of 53.6 per cent of these stars have C/O < 0.8 and Mg/Si > 1 values, suggesting that these stars may potentially host exoplanets that would have compositions akin to planets found within our own Solar system, including both known exoplanet-hosting stars WASP-61 and TOI-754. Both WASP-61 and TOI-754 however are only known to host Jupiter-sized worlds that would have significantly different core structures to that of smaller super-Earth and sub-Neptune exoplanets (Mocquet et al. 2014; Fortney & Nettelmann 2010; Buhler et al. 2016). However, future studies may discover smaller worlds around these stars. Within our GALAH-*TESS* sample, 46.4 per cent of stars have Mg/Si and C/O ratios suggesting that these stars could possibly host rocky planets that are 'silicon-rich' compared to planets found within our Solar system. The candidate exoplanet host TOI-1031 is such a system that could boast Silicon-rich worlds with an Mg/Si value of 0.91 ± 0.20.

Distributions of Mg/Si similar to the ones we find within our sample have also been discovered with other surveys: ∼60 per cent of the Brewer & Fischer (2016) sample of FGK dwarfs in the local neighbourhood also falls between 1 < Mg/Si. Photospheric measurements of planet-hosting stars show a range of Mg/Si values ranging from 0.7 to 1.4 (Delgado Mena et al. 2010; Brewer & Fischer 2016), while our planet host and candidate stars Mg/Si values range from 0.9 to 1.1. Our median Mg/Si value is 0.98 ± 0.22 which is lower than Brewer & Fischer (2016)'s Mg/Si median value of 1.02. The larger spread of Mg/Si values in other surveys might be due to different Solar normalizations but seems more likely that this is due to a different stellar sample and methodologies to derive chemical abundances. Hinkel et al. (2014) showed that even for iron, the spread in for the same stars gathered from various groups was 0.16 dex. Thus, more work is needed to better understand the underlying systematics and variations of stellar abundances from various surveys and research groups (Hinkel et al. 2016; Jofré et al. 2017; Jofré, Heiter & Soubiran 2019).

Surprisingly, less than 1 per cent of GALAH–*TESS* stars have a C/O ratio greater than 0.8, suggesting that these stars may host

'Carbon-Rich' worlds, that will have geological structures unlike any object within our Solar system. Our median C/O value is 0.44 ± 0.13 which is somewhat comparable to other stellar surveys (Delgado Mena et al. 2010; Petigura & Marcy 2011; Amarsi et al. 2016a; Brewer & Fischer 2016; Suárez-Andrés et al. 2018) and population statistics (Fortney 2012) – but could be an overestimate from galactic chemical evolution models (Fortney 2012). The discrepancies between these surveys are likely due to different stellar populations, methodologies used to derive stellar abundances, the single C line used in GALAH DR2 (658.761 nm), or Solar normalizations used as discussed in Section 3.2.

We should note that GALAH's [O/H] abundances do account for non-LTE effects but are only taken from the triplet O_I lines near ∼777.5 nm (Amarsi et al. 2016a; Buder et al. 2018; Gao et al. 2018). This triplet is known to over-estimate abundances if non-LTE effects are not taken into account (Teske et al. 2013). Brewer & Fischer (2016)'s approach considers molecular OH lines and numerous more carbon lines, such that our results might be overestimated with respect to theirs. Teske et al. (2014) found that there is currently no significant trend between planet hosts, in particular the occurrence of hot-Jupiters, and their C/O values.

4.2.3 How are stellar abundances linked to planetary formation?

There is theoretical evidence suggesting that the abundance ratios of refractory materials stay relatively constant throughout a proto-planetary disc, but it is misleading to suggest that volatile abundance ratios will be constant through the disc. This evidence includes the fact that the relative ratios of many elements in the protoplanetary disc do not change during planet formation, including the dominant rocky-planet-building elements: Fe, Mg, and Si (Bond et al. 2010b; Thiabaud et al. 2015). For example, 95 per cent of all atoms in the Earth can be accounted for via Fe, Mg, and Si, along with the constituent oxygen brought in their oxide forms (e.g. rocks containing Mg as MgO, Si as SiO_2 etc., McDonough 2003). In addition, the Sun, Earth, and Mars all agree to within 10 per cent in the relative proportions of the major rocky planet building elements (Waenke & Dreibus 1988; Lodders 2003; McDonough 2003). Mercury, due to its high CMF, does not follow the same similarity; however, stellar abundances can better help us classify planets as Mercury like. Recent work by Schulze et al. (2020) confirms that the molar ratios for refractory elements will be similar for rocky worlds and their host stars. But, work done by Plotnykov & Valencia (2020) contradicts this result, showing that the composition of rocky worlds likely spans a greater range than their host stars. Now with Adibekyan et al. (2021) showing that there might be a linear relationship with a planet's composition and that of its host-star, this assumption is starting to weaken.

Elemental abundance ratios can also change through a proto-planetary disc depending upon the concentration of material and temperature profile of the disk (Bond et al. 2010b; Carter-Bond et al. 2012; Unterborn & Panero 2017). There are studies that suggest that estimates of the devolatilization process within a protoplanetary disc could aid in determining the bulk elemental abundances of rocky worlds, assuming they have formed where they are currently situated within their own planetary system (Wang et al. 2019b).

If we want to determine if a world has bulk composition as the earth, studies suggest that the errors with the elemental abundances themselves need to be further refined with uncertainties better than ∼0.04 dex needed for such a comparison (Hinkel & Unterborn 2018; Wang et al. 2019b). Even further, if we want to differentiate between unique planetary structures within a rocky exoplanet population, the
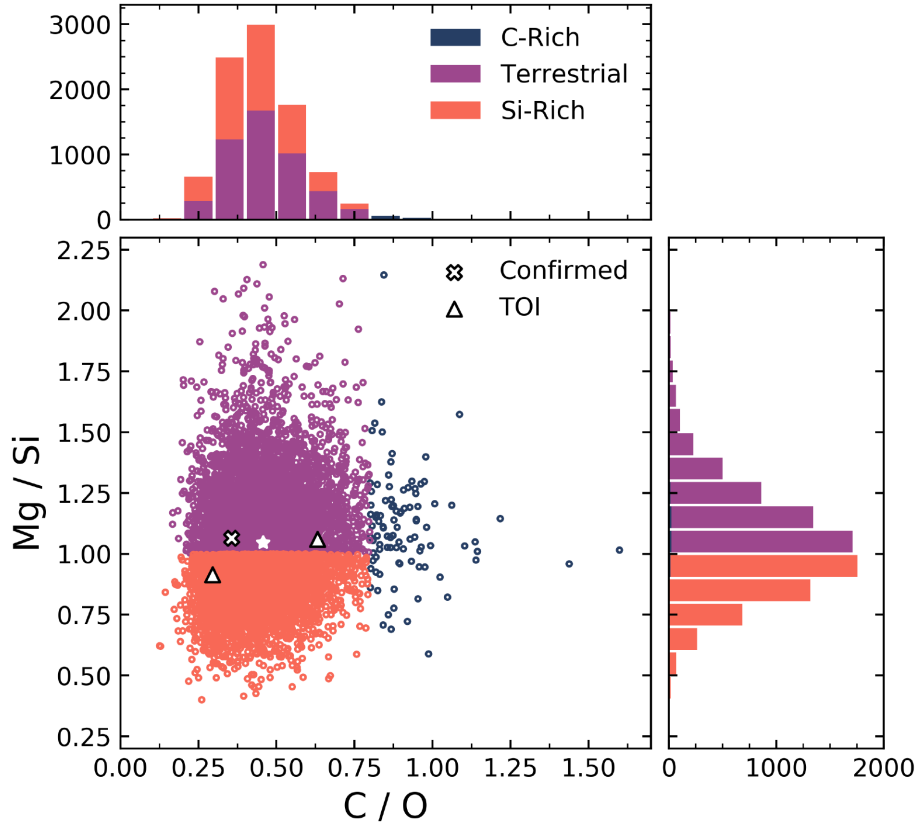
Figure 13. Distribution of all stars that have both measured C/O and Mg/Si ratios. These ratios can help inform astronomers on the likely composition of probable rocky worlds these stars may host. A total of 53.6 per cent of these stars have C/O < 0.8 and Mg/Si > 1 values that would suggest that these stars may potentially host planets that would be similar in geological composition to Earth and Mars. These potential rocky worlds would host olivine and pyroxene within their upper mantle and bridgmanite and magnesiowüstite (or ferropericlase) in their lower mantle. That leaves 46.4 per cent of stars that will host planets unlike any worlds within our Solar system. These include 45.4 per cent of stars potentially hosting 'Silicon-Rich' rocky worlds with stellar abudance ratios C/O < 0.8 and Mg/Si < 1, indicating that these worlds could contain pyroxene + SiO within both their upper and lower mantles. Only 1 per cent of GALAH–*TESS* stars have C/O > 0.8, indicating that they might host rocky worlds with carbon-rich mantles. Planet-hosting (cross) and candidate stars [TOI (upright triangle)] measured Mg/Si and C/O values are displayed on the figure with the Sun's Mg/Si and C/O values depicted with a white star (Lodders et al. 2009).

absolute errors for Fe, Si, Al, Mg, and Ca abundances need to be less than 0.02, 0.01, 0.002, 0.001, and 0.001 dex, respectively (Hinkel & Unterborn 2018). These uncertainties, especially for Al, Mg, and Ca are unobtainable with current detection methods and Solar abundance normalizations. Hence, if we do want to accurately determine an exoplanet's interior and composition, which has vast implications for its habitability, then precision on spectroscopic abundances and Solar normalizations themselves also have to significantly increased.

The relationship between elemental abundances and planetary architectures is a complex one. There is an overall trend that hot-Jupiter systems favour iron-rich hosts (Fischer & Valenti 2005; Mortier et al. 2013) and early evidence that super-Earths are predominantly found around metal-poor and α-rich stars (Adibekyan et al. 2012) and new work with machine-learning algorithms suggest elemental indicators for hot-Jupiter hosting stars apart from Fe are O, C, and Na (Hinkel et al. 2019). The orbits of super-Earths might also be correlated with their host-stars iron abundance, as work by Adibekyan et al. (2013b), Adibekyan, Figueira & Santos (2016), Sousa et al. (2019), and Petigura et al. (2018) shows super-Earths orbiting metal-rich stars have orbits that are shorter than their metal-poor hosted peers.

Sousa et al. (2019) also suggest the mass of planets increases with the host star metallicity, but contradicts Teske et al. (2019), which did not find such a correlation. Brewer et al. (2018) found that compact-multi systems are more common around metal-poor stars, showing

a large [Fe/H] versus Si/Fe parameter space unfilled by single hot-Jupiters but filled with compact-multi systems for planet hosts with [Fe/H] values below 0.2 and Si/Fe values higher than 1.4. Similarly, Adibekyan et al. (2012) also showed that most planets orbiting metal-poor stars are enhanced in alpha elements, leading to higher Si/Fe ratios, and belong to the Milky Way's thick disc.

We have created a similar figure for our small exoplanetary sample, to somewhat forward predict the types of planetary architectures our GALAH–*TESS* stars might host. Fig. 14 shows that the majority of planet hosts and candidates fill quadrant B of this phase-space, where Brewer et al. (2018) found a diverse range of planetary architectures occupying this space. All of our confirmed and candidate systems favour iron-rich, silicon-poor stars, where a diverse range of exoplanetary architectures are likely to be found. This matches our current, though very small sample with single-planet systems hosting sub-Neptune to Jovian-like worlds.

5 CONCLUSION

The aim of this paper is to aid *TESS* follow-up teams with a catalogue of high precision atmospheric, physical and chemical stellar parameters for stars being observed with the space-based exoplanet survey satellite. We have cross-matched GALAH DR2 with the TIC to provide the characteristics for over ∼47 000 stars, eleven of which
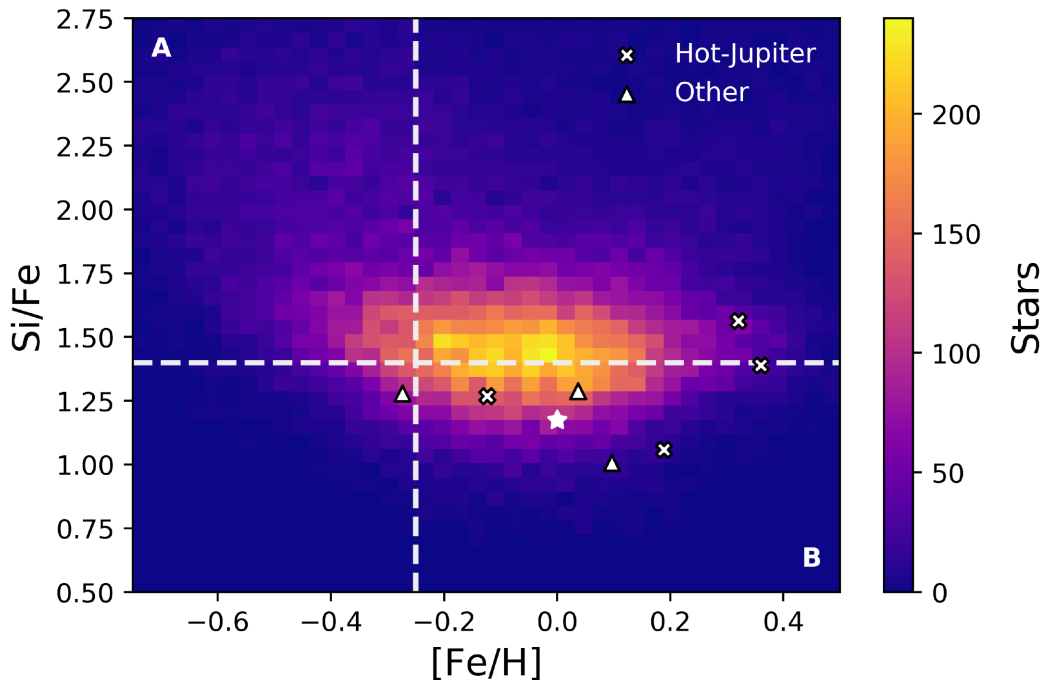
Figure 14. In Brewer et al. (2018), the authors discovered that compact multiplanet systems favoured iron-poor, silicon-rich stars with a higher population of multiplanetary systems favouring the A quadrant in this figure. A wider range of planetary systems, including single-systems consisting of hot-Jupiters were more common within quadrant B of this figure. This figure shows our [Fe/H] and Si/Fe abundance ratios for 43162 GALAH–*TESS* stars. Based upon our results, a more diverse range of planetary systems will be uncovered around GALAH–*TESS* stars, with the majority of our stars lying in quadrant B. The white star represents the Sun's [Fe/H] and Si/Fe values with known confirmed or candidate hot-Jupiter (cross) and other (triangle) planetary systems shown for comparison.

confirmed planet-hosts or planetary candidates discovered by the *TESS* mission. The refinement of stellar radii and masses of those planet-hosting stars have improved the mass and radius measurements of the confirmed and candidate exoplanets they host, with a median relative uncertainty for our planetary mass and radius values being 5 per cent and 4 per cent, respectively. From these refinements, we have increased the planetary radii of CTOI-201256771.01 and CTOI-201256771.02 to near Solar values of $96.17R_\odot$ and $103.15R_\odot$, and with further investigation, have indicated that these transit events were likely caused by the eclipsing binary companion of UNSW-V 320 A. We also cast serious doubts over the candidate events CTOI-220402290.01, CTOI-220402290.02, CTOI-300903537.01, and CTOI 300903537.02 as their orbital periods alone suggest that these candidate systems are likely coming from one source and not two. Our updated mass and radius values changed on the order of 10–20 per cent from literature values, which have minor implications for the large exoplanets currently within the GALAH–*TESS* catalogue, but would have profound impacts on the refinement of a fictitious 'Earth-like' world orbiting these stars, with a range of densities that would render some uninhabitable by current theories of habitability.

Our catalogue contains the elemental abundances for 23 elements that have been normalized by Lodders et al. (2009) to not only drive consistency within the community, but to also make it easier for comparisons of elemental abundances from other abundance driven, stellar surveys to ours. The GALAH–*TESS* catalogue includes the elemental abundance ratios for C/O, Mg/Si, Fe/Mg, and Fe/Si which can help astronomers and planetary scientists make predictions about the composition and structure of potential rocky worlds orbiting our GALAH–*TESS* stars. Our stellar C/O and Mg/Si distributions suggest that the majority of GALAH-*TESS* stars will likely host worlds similar in composition to that of Earth and Mars, with

over 54 per cent of stars hosting Mg/Si > 1, and C/O < 0.8. However, 46 per cent of stars have atmospheric abundance ratios of either Mg/Si < 1 and C/O < 0.8 or C/O > 0.8, suggesting that these stars may host rocky worlds with geological compositions unlike any planet found within our Solar system. These values will change dependent upon the Solar normalization used, hence the need for a standard Solar normalization within the exoplanetary community. It is important in our language that a truly Earth-like planet has yet to be discovered (Tasker et al. 2017). But our characterization of GALAH stars being observed by *TESS* might one day be used to determine the composition of a world just like ours.

SOFTWARE

ACKNOWLEDGEMENTS

contract with the National Aeronautics and Space Administration under the Exoplanet Exploration Program

DATA AVAILABILITY

The data underlying this article are available in Data Central at https://datacentral.org.au/.

REFERENCES

Addison B. C. et al., 2021, MNRAS, 502, 3704
Addison B. et al., 2019, PASP, 131, 115003
Adibekyan V., Figueira P., Santos N. C., 2016, Origins Life Evolution Biosphere, 46, 351
Adibekyan V., Gonçalves da Silva H. M., Sousa S. G., Santos N. C., Delgado Mena E., Hakobyan A. A., 2017, ApJ, 60, 325
Adibekyan V. et al., 2021, preprint (arXiv:2102.12444)
Adibekyan V. Z. et al., 2012, A&A, 543, A89
Adibekyan V. Z. et al., 2013a, A&A, 554, A44
Adibekyan V. Z. et al., 2013b, A&A, 560, A51
Alibert Y., 2014, A&A, 561, A41
Amarsi A. M., Asplund M., 2017, MNRAS, 464, 264
Amarsi A. M., Asplund M., Collet R., Leenaarts J., 2016a, MNRAS, 455, 3735
Amarsi A. M., Lind K., Asplund M., Barklem P. S., Collet R., 2016b, MNRAS, 463, 1518
Anders E., Grevesse N., 1989, Geochim. Cosmochim. Acta, 53, 197
Asplund M., Grevesse N., Sauval A. J., 2005, in Barnes T. G., III, Bash F. N., eds, The Solar Chemical Composition. Astronomical Society of the Pacific Conference Series, San Francisco, p. 25
Asplund M., Grevesse N., Sauval A. J., Scott P., 2009, ARA&A, 47, 481
Astropy Collaboration et al., 2013, A&A, 558, A33
Barclay T., Pepper J., Quintana E. V., 2018, ApJS, 239, 2
Barclay T. et al., 2013, ApJ, 768, 101
Batalha N. M. et al., 2013, ApJS, 204, 24
Benz W., Anic A., Horner J., Whitby J. A., 2007, Space Sci. Rev., 132, 189
Bitsch B., Battistini C., 2020, A&A, 633, A10
Bond J. C., Lauretta D. S., O'Brien D. P., 2010a, Icarus, 205, 321
Bond J. C., O'Brien D. P., Lauretta D. S., 2010b, ApJ, 715, 1050
Bonomo A. S. et al., 2019, Nature Astron., 3, 416
Borucki W. J. et al., 2010, Science, 327, 977
Brewer J. M., Fischer D. A., 2016, ApJ, 831, 20
Brewer J. M., Fischer D. A., Madhusudhan N., 2017, AJ, 153, 83
Brewer J. M., Wang S., Fischer D. A., Foreman-Mackey D., 2018, ApJ, 867, L3
Brugger B., Mousis O., Deleuil M., Deschamps F., 2017, ApJ, 850, 93
Brugger B., Mousis O., Deleuil M., Ronnet T., 2018, Characterizing the deviations of Mercury's bulk composition from solar abundances. European Planetary Science Congress, Berlin, p. EPSC2018–404
Brugman K. K., Phillips M. G., Till C. B., 2019, Experimental Determination of Rocky Exoplanet Crust Compositions. AGU Fall Meeting Abstracts, San Francisco, p. 3016
Buchhave L. A., Latham D. W., 2015, ApJ, 808, 187
Buchhave L. A. et al., 2014, Nature, 509, 593
Buder S. et al., 2018, MNRAS, 478, 4513
Buhler P. B., Knutson H. A., Batygin K., Fulton B. J., Fortney J. J., Burrows A., Wong I., 2016, ApJ, 821, 26
Butters O. W. et al., 2010, A&A, 520, L10
Carrillo A., Hawkins K., Bowler B. P., Cochran W., Vanderburg A., 2020, MNRAS, 491, 4365
Carter-Bond J. C., O'Brien D. P., Delgado Mena E., Israelian G., Santos N. C., González Hernández J. I., 2012, ApJ, 747, L2
Chen J., Kipping D., 2017, ApJ, 834, 17
Choi J., Dotter A., Conroy C., Cantiello M., Paxton B., Johnson B. D., 2016, ApJ, 823, 102
Christiansen J. L. et al., 2008, MNRAS, 385, 1749
Coughlin J. L. et al., 2016, ApJS, 224, 12
Cui X.-Q. et al., 2012, Res. Astron. Astrophys., 12, 1197
Dalba P. A. et al., 2020, AJ, 159, 241
Davis A. B. et al., 2020, AJ, 160, 229
Delgado Mena E., Israelian G., González Hernández J. I., Bond J. C., Santos N. C., Udry S., Mayor M., 2010, ApJ, 725, 2349
De Silva G. M. et al., 2015, MNRAS, 449, 2604
Dorn C., Harrison J. H. D., Bonsor A., Hands T. O., 2019, MNRAS, 484, 712
Dorn C., Hinkel N. R., Venturini J., 2017b, A&A, 597, A38
Dorn C., Khan A., Heng K., Connolly J. A. D., Alibert Y., Benz W., Tackley P., 2015, A&A, 577, A83
Dorn C., Venturini J., Khan A., Heng K., Alibert Y., Helled R., Rivoldini A., Benz W., 2017a, A&A, 597, A37
Duffy T., Madhusudhan N., Lee K., 2015, in Schubert G., ed., Treatise on Geophysics (Second Edition), 2nd edn. Elsevier, Oxford, p. 149
Eisner N. et al., 2020, MNRAS, 494, 750
Elkins-Tanton L. T., Seager S., 2008, ApJ, 685, 1237
Endl M. et al., 2016, ApJ, 818, 34
Feroz F., Hobson M. P., 2008, MNRAS, 384, 449
Feroz F., Hobson M. P., Bridges M., 2009, MNRAS, 398, 1601
Feroz F., Hobson M. P., Cameron E., Pettitt A. N., 2019, OJAp, 2, 10
Fischer D. A., Valenti J., 2005, ApJ, 622, 1102
Fischer D. A. et al., 2008, ApJ, 675, 790
Fortney J. J., 2012, ApJ, 747, L27

Fortney J. J., Nettelmann N., 2010, Space Sci. Rev., 152, 423
Fuhrmann K., 1998, A&A, 338, 161
Gaia Collaboration et al., 2018, A&A, 616, A1
Gao X. et al., 2018, MNRAS, 481, 2666
Gilbert E. A. et al., 2020, AJ, 160, 116
Gillon M. et al., 2017, Nature, 542, 456
Ginsburg A. et al., 2019, AJ, 157, 98
Gonzalez G., 1997, MNRAS, 285, 403
Grevesse N., Asplund M., Sauval A. J., 2007, Space Sci. Rev., 130, 105
Grevesse N., Sauval A. J., 1998, Space Sci. Rev., 85, 161
Hardegree-Ullman K. K., Zink J. K., Christiansen J. L., Dressing C. D., Ciardi D. R., Schlieder J. E., 2020, ApJS, 247, 28
Harris C. R. et al., 2020, Nature, 585, 357
Hellier C. et al., 2012, MNRAS, 426, 739
Hinkel N. R., Burger D., 2017a, preprint (arXiv:1712.04944)
Hinkel N. R., Burger D., 2017b, preprint (arXiv:1712.04944)
Hinkel N. R., Timmes F. X., Young P. A., Pagano M. D., Turnbull M. C., 2014, AJ, 148, 54
Hinkel N. R., Unterborn C., Kane S. R., Somers G., Galvez R., 2019, ApJ, 880, 49
Hinkel N. R., Unterborn C. T., 2018, ApJ, 853, 83
Hinkel N. R. et al., 2016, ApJS, 226, 4
Hirose K., Labrosse S., Hernlund J., 2013, AREPS, 41, 657
Horner J., Jones B. W., 2010, IJAsB, 9, 273
Horner J. et al., 2020, PASP, 132, 102001
Huang C. X. et al., 2018, ApJ, 868, L39
Huber D. et al., 2019, AJ, 157, 245
Hunter J. D., 2007, CSE, 9, 90
Jofré P., Das P., Bertranpetit J., Foley R., 2017, MNRAS, 467, 1140
Jofré P., Heiter U., Soubiran C., 2019, ARA&A, 57, 571
Johns D., Marti C., Huff M., McCann J., Wittenmyer R. A., Horner J., Wright D. J., 2018, ApJS, 239, 14
Johnson J. A. et al., 2011, ApJS, 197, 26
Jones M. I. et al., 2016, A&A, 590, A38
Jordán A. et al., 2020, AJ, 159, 145
Kite E. S., Ford E. B., 2018, ApJ, 864, 75
Kopparapu R. K. et al., 2013, ApJ, 765, 131
Kos J. et al., 2017, MNRAS, 464, 1259
Kuchner M. J., Seager S., 2005, preprint(astro-ph/0504214)
Latham D. W., Mazeh T., Stefanik R. P., Mayor M., Burki G., 1989, Nature, 339, 38
Lawton A. T., Wright P., 1989, J. Br. Interplanet. Soc., 42, 335
Lewis I. J. et al., 2002, MNRAS, 333, 279
Ligi R. et al., 2019, A&A, 631, A92
Lingam M., Loeb A., 2019, Int. J. Astrobiol., 18, 112
Lodders K., 2003, ApJ, 591, 1220
Lodders K., Palme H., Gail H. P., 2009, Landolt Börnstein, 4B, 712
Lovis C., Fischer D., 2010, in Seager S., ed., Exoplanets. University of Arizona Press, Tucson, p. 27
Lovis C. et al., 2011, A&A, 528, A112
Madhusudhan N., Lee K. K. M., Mousis O., 2012, ApJ, 759, L40
Martell S. et al., 2020, preprint (arXiv:2006.02106)
Martell S. L. et al., 2016, MNRAS, 465, 3203
Mayor M., Queloz D., 1995, Nature, 378, 355
McDonough W. F., 2003, TrGeo, 2, 568
McDonough W. F., Sun S. s., 1995, Chem. Geol., 120, 223
McKerns M. M., Strand L., Sullivan T., Fang A., Aivazis M. A., 2012, preprint (arXiv:1202.1056)
McKinney W., 2010, Data Structures for Statistical Computing in Python. Proc. 9th Python in Science Conference, Austin, p. 51
Miozzi F., Morard G., Antonangeli D., Clark A. N., Mezouar M., Dorn C., Rozel A., Fiquet G., 2018, J. Geophys. Res. Planets, 123, 2295
Mocquet A., Grasset O., Sotin C., 2014, RSPTA, 372, 20130164
Mordasini C. et al., 2011, A&A, 526, A111
Moriarty J., Madhusudhan N., Fischer D., 2014, ApJ, 787, 81
Mortier A., Santos N. C., Sousa S. G., Adibekyan V. Z., Delgado Mena E., Tsantaki M., Israelian G., Mayor M., 2013, A&A, 557, A70
Morton T. D., 2015, Astrophysics Source Code Library, record ascl:1503.010

Muirhead P. S. et al., 2012, ApJ, 747, 144
Naef D. et al., 2001, A&A, 375, L27
Ness M., Hogg D. W., Rix H. W., Ho A. Y. Q., Zasowski G., 2015, ApJ, 808, 16
Nielsen L. D. et al., 2019a, MNRAS, 489, 2478
Nielsen L. D. et al., 2019b, A&A, 623, A100
Nisr C., Meng Y., MacDowell A. A., Yan J., Prakapenka V., Shim S.-H., 2017, JGRE, 122, 124
Nittler L. R., Chabot N. L., Grove T. L., Peplowski P. N., 2017, preprint (arXiv:1712.02187)
Noack L., Snellen I., Rauer H., 2017, Space Sci. Rev., 212, 877
Noyes R. W. et al., 2008, ApJ, 673, L79
Osborn A., Bayliss D., 2019, MNRAS, 491, 4481
Osorio Y., Barklem P. S., 2016, A&A, 586, A120
Osorio Y., Barklem P. S., Lind K., Belyaev A. K., Spielfiedel A., Guitou M., Feautrier N., 2015, A&A, 579, A53
Petigura E. A., Marcy G. W., 2011, ApJ, 735, 41
Petigura E. A. et al., 2018, AJ, 155, 89
Plotnykov M., Valencia D., 2020, MNRAS, 499, 932
Putirka K. D., Rarick J. C., 2019, Am. Mineral., 104, 817
Recio-Blanco A. et al., 2014, A&A, 567, A5
Reddy B. E., Lambert D. L., Allende Prieto C., 2006, MNRAS, 367, 1329
Ricker G. R. et al., 2014, J. Astron. Telesc. Instr. Syst., 1, 1
Rogers L. A., Seager S., 2010, ApJ, 712, 974
Rowe J. F. et al., 2014, ApJ, 784, 45
Salaris M., Chieffi A., Straniero O., 1993, ApJ, 414, 580
Santerne A. et al., 2014, A&A, 571, A37
Santos N. C., Israelian G., Mayor M., 2001, A&A, 373, 1019
Schubert G., Anderson J. D., Travis B. J., Palguta J., 2007, Icarus, 188, 345
Schulze J. G., Wang J., Johnson J. A., Gaudi B. S., Unterborn C. T., Panero W. R., 2020, preprint (arXiv:2011.08893)
Seager S., Kuchner M., Hier-Majumder C. A., Militzer B., 2007, ApJ, 669, 1279
Shallue C. J., Vanderburg A., 2018, AJ, 155, 94
Sharma S. et al., 2018, MNRAS, 473, 2004
Sharma S. et al., 2019, MNRAS, 490, 5335
Sheinis A. et al., 2015, JATIS, 1, 035002
Skrutskie M. F. et al., 2006, AJ, 131, 1163
Smith A. M. S. et al., 2012, MNRAS, 426, 739
Sousa S. G. et al., 2019, MNRAS, 485, 3981
Stassun K. G., Collins K. A., Gaudi B. S., 2017, AJ, 153, 136
Stassun K. G. et al., 2018, AJ, 156, 102
Stassun K. G. et al., 2019, AJ, 158, 138
Steinmetz M. et al., 2006, AJ, 132, 1645
Suárez-Andrés L., Israelian G., González Hernández J. I., Adibekyan V. Z., Delgado Mena E., Santos N. C., Sousa S. G., 2018, A&A, 614, A84
Suissa G., Chen J., Kipping D., 2018, MNRAS, 476, 2613
Sullivan P. W. et al., 2015, ApJ, 809, 77
Tasker E. et al., 2017, NatAs, 1, 0042
Taylor M. B., 2005, TOPCAT & STIL: Starlink Table/VOTable Processing Software. Astronomical Data Analysis Software and Systems XIV ASP Conference Series, San Francisco, p. 29
Teske J. K., Cunha K., Schuler S. C., Griffith C. A., Smith V. V., 2013, ApJ, 778, 132
Teske J. K., Cunha K., Smith V. V., Schuler S. C., Griffith C. A., 2014, ApJ, 788, 39
Teske J. K., Thorngren D., Fortney J. J., Hinkel N., Brewer J. M., 2019, AJ, 158, 239
Thiabaud A., Marboeuf U., Alibert Y., Cabral N., Leya I., Mezger K., 2014a, A&A, 562, A27
Thiabaud A., Marboeuf U., Alibert Y., Cabral N., Leya I., Mezger K., 2014b, A&A, 562, A27
Thiabaud A., Marboeuf U., Alibert Y., Leya I., Mezger K., 2015, A&A, 580, A30
Torres G. et al., 2015, ApJ, 800, 99

Unterborn C. T., Desch S. J., Hinkel N. R., Lorenzo A., 2018a, Nature Astron., 2, 297

Unterborn C. T., Desch S. J., Panero W. R., 2018b, Fall Meeting 2018. American Geophysical Union, Washington D.C., p. P42A

Unterborn C. T., Dismukes E. E., Panero W. R., 2016, ApJ, 819, 32

Unterborn C. T., Kabbes J. E., Pigott J. S., Reaman D. M., Panero W. R., 2014, ApJ, 793, 124

Unterborn C. T., Panero W. R., 2017, ApJ, 845, 61

Unterborn C. T., Panero W. R., 2019, JGRE, 124, 1704

Valencia D., O'Connell R. J., Sasselov D., 2006, Icarus, 181, 545

Valenti J. A., Piskunov N., 1996, A&AS, 118, 595

Vanderspek R. et al., 2019, ApJ, 871, L24

van der Walt S., Colbert S. C., Varoquaux G., 2011, CSE, 13, 22

Virtanen P. et al., 2020, NatMe, 17, 261

Vogt S. S. et al., 2010, ApJ, 708, 1366

Waenke H., Dreibus G., 1988, RSPTA, 325, 545

Wang H. S., Liu F., Ireland T. R., Brasser R., Yong D., Lineweaver C. H., 2019b, MNRAS, 482, 2222

Wang Q., Zhang X., Zhang Y., Yi Q., 2013, AUGEM: automatically generate high performance dense linear algebra kernels on x86 CPUs. Proceedings of the International Conference on High Performance Computing, Networking, Storage and Analysis, Denver, p. 1

Wang S. et al., 2019a, AJ, 157, 51

Wanke H., Dreibus G., 1994, RSPTA, 349, 285

Wilson H. F., Militzer B., 2014, ApJ, 793, 34

Wittenmyer R. A. et al., 2014, ApJ, 783, 103

Wittenmyer R. A. et al., 2017, AJ, 154, 274

Wittenmyer R. A. et al., 2018, AJ, 155, 84

Wittenmyer R. A. et al., 2020, MNRAS, 491, 5248

Wolszczan A., Frail D. A., 1992, Nature, 355, 145

Xianyi Z., Qian W., Yunquan Z., 2012, Model-driven Level 3 BLAS Performance Optimization on Loongson 3A Processor. IEEE 18th International Conference on Parallel and Distributed Systems, Washington D.C., p. 684

Zeng L., Sasselov D. D., Jacobsen S. B., 2016, ApJ, 819, 127

Zolotov M. Y., Tobie G., Postberg F., Magee B., Waite J. H., Esposito L., 2011, Chemical and Phase Composition of Enceladus: Insights from Cassini Observations. EPSC-DPS Joint Meeting 2011, Nantes, p. 1330

APPENDIX A

See Table A1.

Table A1. Column names, units, data types and descriptions for the GALAH-*TESS* parameters table.

Name	Units	Data type	Description
TIC_ID		int64	*TESS* Input Catalog (TIC) Identifier
TWOMASS		int64	Two Micron All-Sky Survey (2MASS) identifier
GAIADR2		long64	*Gaia* DR2 Identifier
PRIORITY		float64	TIC v8 priority
RA	deg	float64	J2000 right ascension from 2MASS
DEC	deg	float64	J2000 declination from 2MASS
TEFF	K	int64	GALAH DR2 Effective temperature
E_TEFF	K	int64	Uncertainty in TEFF
LOGG	dex	float64	GALAH DR2 Surface gravity
E_LOGG	dex	float64	Uncertainty in LOGG
M_H	dex	float64	GALAH DR2 overall metallicity
E_MH	dex	float64	Uncertainty in M_H
ALPHA_FE	dex	float64	[α/Fe] abundance
E_ALPHA_FE	dex	float64	Uncertainty in ALPHA_FE
VMAG	mag	float64	V magnitude from TIC
E_VMAG	mag	float64	Uncertainty in VMAG
TMAG	mag	float64	*TESS* magnitude from TIC
E_TMAG	mag	float64	Uncertainty in TMAG
HMAG	mag	float64	2MASS H magnitude from TIC
E_HMAG	mag	float64	Uncertainty in HMAG
JMAG	mag	float64	2MASS J magnitude from TIC
E_JMAG	mag	float64	Uncertainty in JMAG
KMAG	mag	float64	2MASS K magnitude from TIC
E_KMAG	mag	float64	Uncertainty in KMAG
GMAG	mag	float64	*Gaia* G magnitude from TIC
E_GMAG	mag	float64	Uncertainty in GMAG
GRPMAG	mag	float64	*Gaia* G_RP magnitude from TIC
E_GRPMAG	mag	float64	Uncertainty in GRPMAG
GBPMAG	mag	float64	*Gaia* G_BP magnitude from TIC
E_GBPMAG	mag	float64	Uncertainty in GBPMAG
PLX	mas	float64	Parallax from TIC
E_PLX	mas	float64	Uncertainty in PLX
DIST	pc	float64	Distance from TIC
E_DIST	pc	float64	Uncertainty in DIST
RADIUS	$R_\odot$	float64	isochrone Stellar radius
E_RADIUS	$R_\odot$	float64	Uncertainty in RADIUS
MASS	$M_\odot$	float64	isochrone Stellar mass
E_MASS	$M_\odot$	float64	Uncertainty in MASS
RHO	gcm^{-3}	float64	isochrone Stellar density
E_RHO	gcm^{-3}	float64	Uncertainty in RHO
LUM	$L_\odot$	float64	Stellar luminosity
E_LUM	$L_\odot$	float64	Uncertainty in LUM
AGE	Gyr	float64	isochrone Stellar age
E_AGE	Gyr	float64	Uncertainty in AGE
EEP		int64	MIST isochrone equivalent evolutionary phase
E_EEP		int64	Uncertainty in EEP
RV	$km\,s^{-1}$	float64	GALAH DR2 Radial velocity from internal cross-correlation against data
E_RV	$km\,s^{-1}$	float64	Uncertainty in RV
VSINI	$km\,s^{-1}$	float64	GALAH DR2 Line of sight rotational velocity
E_VSINI	$km\,s^{-1}$	float64	Uncertainty in VSINI
VMIC	$km\,s^{-1}$	float64	GALAH DR2 Microturbulence velocity
E_VMIC	$km\,s^{-1}$	float64	Uncertainty in VMIC
HZRECVEN	au	float64	Recent Venus Habitable Zone
HZRUNGRN	au	float64	Runaway Greenhouse Habitable Zone
HZMOIGRN	au	float64	Moist Greenhouse Habitable Zone
HZMAXGRN	au	float64	Maximum Greenhouse Habitable Zone
HZEARMAR	au	float64	Early Mars Habitable Zone
X_H	dex	float64	[X/H] abundance for element X
E_X_H	dex	float64	[X/H] Uncertainty in X_H
C_O		float64	(C/O) abundance ratio
E_C_O		float64	Uncertainty in C_O
MG_SI		float64	(Mg/Si) abundance ratio
E_MG_SI		float64	Uncertainty in MG_SI
FE_MG		float64	(Fe/Mg) abundance ratio
E_FE_MG		float64	Uncertainty in FE_MG
FE_SI		float64	(Fe/Si) abundance ratio
E_FE_SI		float64	Uncertainty in FE_SI

This paper has been typeset from a TEX/LATEX file prepared by the author.